

Current Velocity Profiling from an Autonomous Underwater Vehicle with the Application of Kalman Filtering

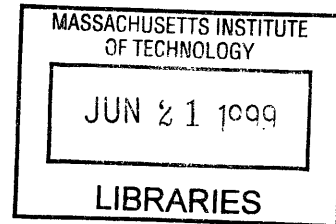
by
Yanwu Zhang

B.S., Electrical Engineering, Northwestern Polytechnic University, China, 1989
M.S., Underwater Acoustics Engineering, Northwestern Polytechnic University, China, 1991

Submitted to the Department of Ocean Engineering of MIT
and
the Department of Applied Ocean Physics and Engineering of WHOI
and
the Department of Electrical Engineering and Computer Science of MIT
in partial fulfillment of the requirements for the degrees of

MASTER OF SCIENCE
IN OCEANOGRAPHIC ENGINEERING
at the
MASSACHUSETTS INSTITUTE OF TECHNOLOGY
and the
WOODS HOLE OCEANOGRAPHIC INSTITUTION
and

MASTER OF SCIENCE
IN ELECTRICAL ENGINEERING AND COMPUTER SCIENCE
at the
MASSACHUSETTS INSTITUTE OF TECHNOLOGY



Eng

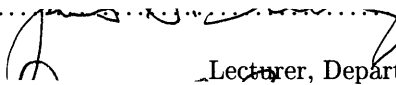
September 1998

© Massachusetts Institute of Technology and Woods Hole Oceanographic Institution, 1998. All rights reserved.


Author

Joint Program in Applied Ocean Science and Engineering,
Massachusetts Institute of Technology/ Woods Hole Oceanographic Institution,
and Department of Electrical Engineering and Computer Science,
Massachusetts Institute of Technology
August 3, 1998


Certified by


James G. Bellingham
Lecturer, Department of Ocean Engineering, MIT
Thesis Supervisor


Certified by


Arthur B. Baggeroer
Professor, Department of Ocean Engineering
and Department of Electrical Engineering and Computer Science, MIT
Thesis Supervisor

Accepted by


Michael S. Triantafyllou
Chairman, Joint Committee for Applied Ocean Science and Engineering
Massachusetts Institute of Technology/ Woods Hole Oceanographic Institution

Accepted by


Arthur C. Smith
Chairman, Committee on Graduate Students,
Department of Electrical Engineering and Computer Science, MIT

**Current Velocity Profiling from an Autonomous Underwater Vehicle
with the Application of Kalman Filtering**

by
Yanwu Zhang

Submitted to the Department of Ocean Engineering of MIT
and
the Department of Applied Ocean Physics and Engineering of WHOI
and
the Department of Electrical Engineering and Computer Science of MIT
on August 3, 1998, in partial fulfillment of the requirements for the degrees of
Master of Science in Oceanographic Engineering
and
Master of Science in Electrical Engineering and Computer Science

Abstract

The thesis presents data processing schemes for extracting Earth-referenced current velocity from relative current velocity measurement made by an Acoustic Doppler Current Profiler (ADCP) borne by an Autonomous Underwater Vehicle (AUV). Compared with conventional approaches, current profiling from an AUV platform has advantages including three-dimensional mobility, rapid response, high-level intelligent control, independence from ship motion and weather constraint, and shallow water operation. First, an acausal post-processing scheme is presented for estimating the AUV's own velocity and removing it from the relative velocity measurement to obtain the true current velocity. Then, a causal scheme for estimating the Earth-referenced current velocity is presented. The causal algorithm is based on an Extended Kalman Filter (EKF) that utilizes the hydrodynamics connecting current velocity to vehicle's motion. In both methods, the raw ADCP measurement is corrected to achieve more accurate current velocity estimate. Field data from the Haro Strait Tidal Front Experiment are processed by both methods. Current velocity estimation results reveal horizontal and vertical velocity structure of the tidal mixing process, and are also consistent with the vehicle's deviated trajectory. The capability of the AUV-borne current profiling system is thus demonstrated.

Thesis Supervisor: James G. Bellingham
Title: Lecturer, Department of Ocean Engineering, MIT

Thesis Supervisor: Arthur B. Baggeroer
Title: Professor, Department of Ocean Engineering and Department of Electrical Engineering and Computer Science, MIT

Acknowledgments

First I would like to express my sincere gratitude to my thesis supervisors, Dr. James Bellingham and Prof. Arthur Baggeroer, for their precious guidance. I thank Jim and Art for their thorough yet quick review of my thesis draft despite their pressing schedules. I am grateful to my WHOI advisor Dr. Albert (Sandy) Williams III for his support and advice. I am also grateful to my former advisors, Prof. Chryssostomos Chryssostomidis and Prof. Jerome Milgram for supervising me. I thank Prof. Henrik Schmidt for his support during the Haro Strait Experiment. I feel so lucky to be introduced into MIT Sea Grant AUV Lab, a lab featuring deep-water pressure and uplifting buoyancy. Conversations with Jim have helped me through the past three years and let me learn many things even including technical writing skills. In both of his offices, Chrys has given me important supervision and friendly support. This work was funded by the Office of Naval Research (ONR) under Grants N00014-95-1-1316, N00014-95-1-0495, and ONR/RD Instruments (RDI) Contract No. 785665 under Prime Contract N00014-95-C-0407, and by MIT Sea Grant College Program under Grant NA46RG0434. I am thankful to RDI engineers for their help. I deeply appreciate the support and advice from the ONR Program Manager Dr. Thomas Curtin. Part of the thesis work was presented at the 10th ISUUST. I am grateful to Director Richard Blidberg of AUSI and the Review Committee for granting me the Student Paper Competition Award.

My officemate Mr. Scott Willcox did important work in incorporating the ADCP unit into the AUV, and designed the auxiliary electronic board for sending interrupt signals to the ADCP. Scott also helped me with other stuff, including \LaTeX which I use to write this thesis. Sincere thanks to Prof. John Leonard and Dr. Bradley Moran for providing the LBL navigation data and the coordinates of the Haro Strait area, to Dr. James Bales for his sharp critiques and suggestions, to Dr. Ryszard Pawlowicz for providing the tidal current model and bathymetry for Haro Strait. Special thanks to Dr. Moran and Dr. Bales for tolerating my interrupting questions as they work. During the Haro Strait Experiment, Mr. Robert Grieve always reached out helping hands in his unique military style. Working with all you guys is truly a pleasure.

I thank my former advisor Prof. William Wilcock, Prof. Russell McDuff, Prof. John Delaney, Prof. Ronald Merrill, Prof. Paul Johnson, and Prof. Arthur Nowell of University of Washington. I thank Paul & Betty, Ji-yong & Haiyan, Pei & Yanan, Weiran & Guangyu, Leslie, Marilyn, Jeff and other brothers and sisters in the MIT Chinese Bible Study group, and old roommates Nate and Wen. Many thanks to my host family Roger & Alberta for their friendship and help in many ways.

I am grateful to Yanqing for all the unforgettable help, support, and love.

My Dad, Mum, and elder sister Yanwen have been steadfastly behind me all the way. During his visit this summer, Dad cooked tasty meals in the extremely hot kitchen when I prepared for the Part II Doctoral Exam and wrote this thesis. On the other side of the planet, Mum and my sister have not seen me for four years. This thesis is dedicated to all of you.

Contents

- List of Figures** **6**

- List of Tables** **9**

- 1 Introduction** **10**
 - 1.1 Motivation 10
 - 1.2 Background and Existing Work 11
 - 1.3 AUV as Instrument Platform 13
 - 1.4 Thesis Work 14

- 2 Experimental Description** **17**
 - 2.1 Tidal Mixing at Haro Strait 17
 - 2.2 Experimental Area and Grid Coordinate System 19
 - 2.3 ADCP 20
 - 2.4 Long-BaseLine (LBL) Navigation Array 23
 - 2.5 AUV’s Depth Measurement 24
 - 2.6 Heading/Pitch/Roll Measurements of AUV and ADCP 25

- 3 Data Post-Processing Method** **26**
 - 3.1 Data Processing Method 27
 - 3.1.1 Time Synchronization 27
 - 3.1.2 Estimating AUV’s Own Velocity 27
 - 3.1.3 Sources of Errors 27

3.1.4	Corrections of ADCP Measurement	29
3.1.5	Low-Pass Smoothing	35
3.1.6	Extraction of Earth-Referenced Current Velocity	35
3.2	Data Processing Results	35
4	Application of Extended Kalman Filtering	48
4.1	Brief Introduction to Kalman Filtering	48
4.2	Development of Extended Kalman Filter	49
4.2.1	Model Formulation	49
4.2.2	Underlying Nonlinear Dynamics in Horizontal Plane	51
4.2.3	Jacobian Matrix for the Nonlinear State Equation	55
4.2.4	Error Covariance Matrices	57
4.2.5	Parameter Values	60
4.3	Extended Kalman Filtering Procedure and Results	61
4.3.1	Extended Kalman Filtering Procedure	61
4.3.2	Current and AUV Velocity Estimation Results	64
5	Conclusion	72
5.1	Contributions	72
5.2	Future Work	73
	Bibliography	74

List of Figures

1.1	Odyssey IIB AUV with an ADCP at its bottom midsection (courtesy of Dr. James G. Bellingham).	14
2.1	Geography around Haro Strait (based on map data provided by Institute of Ocean Sciences, Canada).	17
2.2	Flood flow at Haro Strait (using a tidal current model provided by Institute of Ocean Sciences, Canada).	19
2.3	Grid coordinate system and bathymetry (in meter) of the experimental area. Four LBL acoustic transponders were deployed as marked by circles.	20
2.4	Bottom view and side view of the RDI ADCP unit.	21
2.5	ADCP's four-beam radial velocity measurement over depth bins.	22
3.1	Block diagram of the data post-processing procedure.	26
3.2	Depth bin numbering correction for ADCP data.	29
3.3	ENU transformation correction for ADCP velocity.	30
3.4	Rotations by heading, pitch, and roll.	30
3.5	Pitch/roll for ADCP's internal sensors and AUV's KVH sensors.	33
3.6	Headings measured by ADCP's internal compass and AUV's KVH compass.	34
3.7	Horizontal trajectory of the AUV during Mission 14 on June 25, 1996.	36
3.8	Vertical trajectory of the AUV during Mission 14 on June 25, 1996.	37
3.9	Raw current velocity measured by the ADCP during Mission 14 on June 25, 1996.	38

3.10	Computation result of Earth-referenced current velocity for Mission 14 on June 25, 1996.	39
3.11	Horizontal current velocity near the AUV and its effect on the AUV's trajectory during Mission 14 on June 25, 1996.	40
3.12	Vertical current velocity along with AUV's CTD measurements during Mission 14 on June 25, 1996.	42
3.13	Horizontal trajectory of the AUV during Mission 11 on June 28, 1996.	43
3.14	Vertical trajectory of the AUV during Mission 11 on June 28, 1996. .	44
3.15	Raw current velocity measured by the ADCP during Mission 11 on June 28, 1996.	45
3.16	Computation result of Earth-referenced current velocity for Mission 11 on June 28, 1996.	46
3.17	Horizontal current velocity near the AUV during Mission 11 on June 28, 1996.	47
4.1	Horizontal plane schematic of AUV velocity and water current velocity, as well as resultant drag forces.	51
4.2	Illustration of drag force analysis in both plan view and side view. . .	53
4.3	Kalman filter loop.	62
4.4	EKF-estimated AUV positions compared with raw measurements made by the LBL navigation system.	65
4.5	EKF-estimated AUV's and current's Earth-referenced velocities compared with raw velocity measurement made by the ADCP.	66
4.6	Time evolution of Kalman Filter estimation errors for AUV's position, AUV's Earth-referenced velocity, and current's Earth-referenced velocity.	67
4.7	Time evolution of cross-correlations for AUV's Earth-referenced velocity pair and current's Earth-referenced velocity pair.	68
4.8	Time evolution of Kalman Filter gains for current's Earth-referenced v_{xc} associated with the 4 measurements: x_m , y_m , v_{mxrel} , and v_{myrel} . .	69

4.9	Time evolution of Kalman Filter gains for current's Earth-referenced v_{yc} associated with the 4 measurements: x_m , y_m , v_{mxrel} , and v_{myrel} .	70
4.10	Earth-referenced horizontal current velocity near the AUV during Mission 11 on June 28, 1996.	71

List of Tables

- 2.1 ADCP settings at Haro Strait. 21
- 2.2 Heading/pitch/roll sensors' accuracy (at tilt angles up to $\pm 20^\circ$) comparison. 25

- 4.1 AUV related parameters 60
- 4.2 Plant noise parameters 60
- 4.3 Measurement noise parameters 61

Chapter 1

Introduction

1.1 Motivation

The thesis addresses the problem of water current velocity profiling from an Autonomous Underwater Vehicle (AUV). Current velocity measurement is a first order task in ocean process research, environmental monitoring, ship traffic control, and other offshore work [1]. On an Odyssey IIB class AUV [2], an Acoustic Doppler Current Profiler (ADCP) is mounted for making long-range current velocity profiles beneath the vehicle. Taking advantage of the AUV's speed and three-dimensional mobility, current velocity profiling can be carried out with much more synopticity and flexibility than by conventional means.

It should be noted that the raw current velocity measured by an AUV-borne ADCP is referenced to the moving platform, but what we typically need is the Earth-referenced current velocity. The platform's own velocity should be removed from the ADCP's raw measurement so that the Earth-referenced current velocity can be extracted. This is a general problem in ADCP applications. The problem is even more challenging for the AUV-borne scenario where the vehicle's cruising speed is typically much larger than the true current velocity and the vehicle's dynamics is complicated. For the experiment presented in this thesis, estimation of the vehicle's own velocity relies solely on acoustic navigation and depth measurement since the ADCP's bottom-track function was not equipped. Actually, in deep ocean surveys,

the seabed is often out of range even if the bottom-track mode is available. Therefore, the working condition of the presented research is demanding but representative.

The thesis describes an AUV-borne current profiling system, and presents methods for recovering the true current velocity. The system was put into use during the summer 1996 Haro Strait Tidal Front Experiment [3]. The presented processing algorithms are applied to the field data. The results are shown to provide insight into the tidal mixing process.

1.2 Background and Existing Work

An ADCP measures the water current velocity utilizing the Doppler principle. It transmits acoustic waves and then receives echoes returning from sound scatterers in the water. The reflected wave bears a frequency shift compared with the transmitted wave. The frequency shift is proportional to the radial velocity of the scatterer, as expressed by Equation (1.1).

$$f_D = 2 \frac{v_r}{c} f_s \quad (1.1)$$

where f_D is the Doppler frequency shift; f_s is the frequency of the transmitted signal; v_r is the radial velocity of the scatterer; c is the sound speed. Note that since the ADCP both transmits and receives, the Doppler frequency shift is doubled compared with one-way propagation.

Based on the frequency difference between the transmitted and the received signals, the velocity of the sound scatterers can be calculated. These scatterers are plankton or other small particles floating in the water. In most cases, the assumption that the scatterers are passively advected by water motion is valid, hence the scatterers' velocity represents that of the water current [4], [5]. Current velocity is thus obtained based on the Doppler principle. Furthermore, an ADCP measures the current velocity over a large depth range which is divided into sequential "depth

bins”. This capability is achieved by the technique of “range gating” [4]. Echoes from far ranges take longer to return to the ADCP than those from close ranges. Range gating breaks the received signal into successive segments which correspond to reflections from increasingly distant depth bins. Current velocity is averaged within the same bin to give the reading. For its ability of making a profile of current velocity over some depth range, the instrument is called “profiler”. Besides water column profiling, bottom-track is the other working mode of an ADCP. In this mode, the ADCP platform’s speed referenced to the bottom can be calculated from the Doppler frequency shift borne by the bottom-reflected echoes. By measuring the time-delay of the echoes, the distance between the ADCP and the bottom is also obtained. When the water bottom is within the range of ADCP, bottom-track is often utilized for measuring the absolute speed of the ADCP’s platform. More technical details of ADCP will be given in Section 2.3.

Compared with older mechanical or electro-magnetic current meters, an ADCP has the advantage of permitting unobstructed flow measurement because it is not physically intrusive and hence does not disturb the water flow. Over the past decade, ADCPs have been mounted on ships, moorings, and the ocean bottom.

Installed in the hulls of surface vessels [6], [7], [8], [9], ADCPs work in a downward-looking orientation to make current velocity profiles of the water below the ship. The ship’s navigation error and the ADCP’s mounting misalignment error are of main concern in estimating the absolute current velocity. The Global Positioning System (GPS) is an asset that a surface ship can utilize for knowing the position and consequently the speed of its own. When the water bottom is within the ADCP’s range, its bottom-track mode can also be used to estimate the ship’s own speed. However, a ship is constrained to the surface, thus the ADCP profiling cannot penetrate some depth bound. Ship time is very expensive too, typically costing around \$20k/day. The use of a Lowered ADCP (LADCP) [10] provides an alternative approach for investigating deep current from a ship. An LADCP is attached to a Conductivity-Temperature-Depth (CTD) rosette package, and lowered down from a surface vessel. It records water velocity during downcasts and upcasts. The unknown motion of

the platform determines that an LADCP is suitable for measuring the vertical shear of current velocity, i.e., the vertical differentiation of velocity which rejects the unwanted platform motion. With the help of the ship's GPS data and some integration techniques, the extraction of the Earth-referenced current velocity is possible.

Free from surface vessels, ADCPs have been mounted on moorings [11], [12], [5] and at the ocean bottom [13]. Either on a mooring or at the sea bottom, the ADCP can only work for monitoring current velocity at spatially fixed locations.

Using an acoustic Doppler device on an underwater vehicle is at its beginning stage. In [14], an ADCP is installed on an Remotely Operated Vehicle (ROV). In this application, however, the ADCP functions only in its bottom-track mode for improving the vehicle's real-time navigation rather than for making current velocity profiles.

1.3 AUV as Instrument Platform

Studying the oceans requires introducing sensors to their interior depths [15], and AUVs have the potential to provide economical and flexible access [2]. An AUV is a mobile instrument platform [15]. Using on-board instruments, AUVs are capable of conducting oceanographic missions without the typical operating constraints associated with weather, sea state, as well as host ship motion and maneuvering requirements [16]. Accordingly, the pace of AUV development has increased substantially during the past two decades [17].

Odyssey IIB AUVs, designed and built by MIT Sea Grant AUV Laboratory, are small and high performance survey platforms [2]. Each vehicle is torpedo-like with a length of 2.15 m, and a diameter of 0.59 m at its largest vertical cross-section, as shown in Figure 1.1. The vehicle has an outer fairing for hydrodynamic stability and drag reduction, and an inner fairing for structural integrity. These structures are free-flooded, except for two 17-inch-diameter glass spheres which provide the main dry volume. The vehicles operate autonomously with its on-board computer and battery system, along with various sensors. They can be deployed with minimal logistical

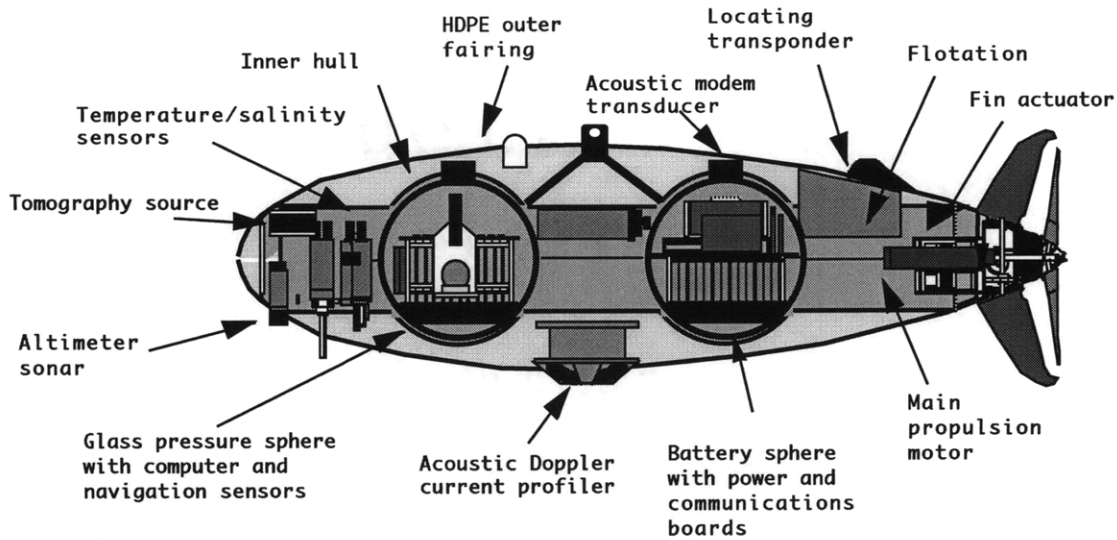


Figure 1.1: Odyssey IIB AUV with an ADCP at its bottom midsection (courtesy of Dr. James G. Bellingham).

support from remote sites, off ships of opportunity, or in rough seas. In the past few years, Odyssey IIB AUVs have fulfilled more than 300 successful missions under the Arctic ice, over the Pacific Ocean ridge, in the Haro Strait tidal current, off the coast of New Zealand, and at the convective Labrador Sea.

1.4 Thesis Work

In the summer of 1996, an RDI Workhorse ADCP was mounted on an Odyssey IIB AUV [18]. The AUV-borne ADCP played a key role in the Haro Strait Tidal Front Experiment which will be elaborated in Chapter 2. As shown in Figure 1.1, the ADCP poses in a downward-looking orientation, at the bottom midsection of the vehicle. Utilizing the AUV's three-dimensional mobility, the ADCP can be used to survey water current in a very flexible manner. Compared with conventional methods, AUV-borne current profiling has advantages including rapid response, high-level intelligent control, independence from ship motion and weather constraint, and shallow water operation. To the author's knowledge, this AUV-borne current profiling system is the first to map current velocity from an AUV. The thesis describes this system and presents the methods for recovering the Earth-referenced current velocity.

At the time of the Haro Strait Experiment, the bottom-track function was not equipped with the Workhorse ADCP provided by RDI. Hence, the vehicle relied on the Long-BaseLine (LBL) sonar beacon array for horizontal navigation, and on the on-board depth sensor for vertical navigation. From the AUV's three-dimensional positioning, the vehicle's velocity is estimated. Velocity of the ADCP's platform is thus removed from the raw current velocity measurement. In this way, the Earth-referenced current velocity is obtained. Data processing techniques include time synchronization between different sensors, ADCP data corrections, and low-pass smoothing for suppressing estimation errors.

Cruising in the current, the AUV's motion is closely related with the water velocity via hydrodynamic forces. The thesis also makes an effort to further utilize the prior knowledge of the vehicle's hydrodynamics for better estimates of the AUV's own velocity as well as the Earth-referenced current velocity. Based on the nonlinearity of the AUV's dynamics, a state space model and an Extended Kalman Filter (EKF) [19], [20] are set up. A causal algorithm for current velocity estimation is developed.

The capability of this AUV-borne current profiling system has been tested through the Haro Strait Tidal Front Experiment. Field data collected by the ADCP combined with the AUV's other measurements are processed. Results reveal shear structure of the horizontal flow, and alternating upwellings and downwellings of the vertical flow. In collaboration with a numerical tide current model of the same region, the current velocity measurements from the AUV have proved to be very helpful for understanding the tidal mixing process. The AUV's role as a mobile and intelligent instrument platform is further demonstrated.

To make clear the application environment of the AUV-borne current profiling system, the Haro Strait Experiment setup and the oceanography context are described in Chapter 2. Working principle of the ADCP and its operation during the Experiment are discussed in detail. The vehicle's LBL navigation system, its depth measurement, as well as the heading/pitch/roll sensors of the AUV and the ADCP are also introduced.

Using the AUV's three-dimensional navigation system, the vehicle's own velocity

is estimated. The platform velocity is then removed from the relative current velocity measurement made by the ADCP, so that the Earth-referenced current velocity is derived. Chapter 3 presents the data post-processing method. Field data from the Haro Strait Tidal Front Experiment are processed, and their physical meanings are discussed.

The algorithm presented in Chapter 4 takes one step forward by making use of the AUV's hydrodynamics information. The motivation comes from the fact that the vehicle's motion is closely related with the water velocity via hydrodynamic forces. A nonlinear state space model is established, and an EKF is developed. The Haro Strait Experiment data are used to test this Kalman Filtering based scheme.

In the end, a summary of contributions and a discussion on future work are given in Chapter 5.

Chapter 2

Experimental Description

2.1 Tidal Mixing at Haro Strait

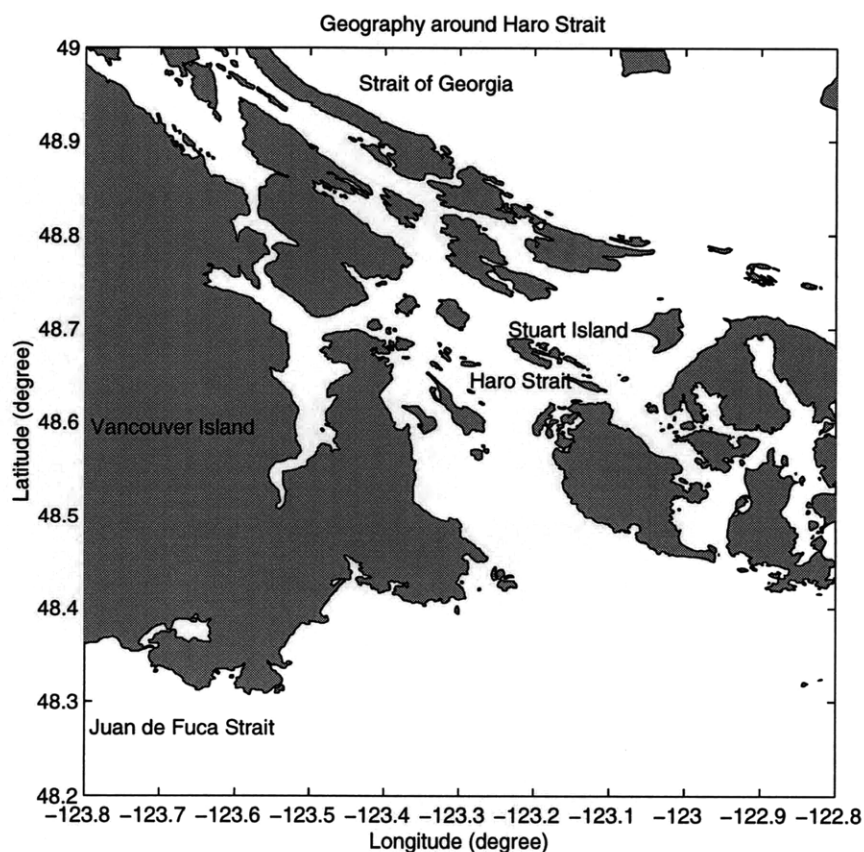


Figure 2.1: Geography around Haro Strait (based on map data provided by Institute of Ocean Sciences, Canada).

The Haro Strait (around $48^{\circ}40'$ N, $123^{\circ}10'$ W) is part of a narrow channel between Washington State of the U. S. and Vancouver Island of British Columbia, Canada. It is the largest channel connecting Strait of Georgia with Juan de Fuca Strait, as shown in Figure 2.1. Fraser River (to the north of 49° N) flows into Strait of Georgia. At Haro Strait, this southward fresh water mixes with salty sea water coming from the Pacific through Juan de Fuca Strait. A front forms at the junction of these two different water masses [21]. Since the mixing of the channel flows is tidally driven, it is called “tidal mixing”.

Tidal mixing is important to many practical problems including dispersion of nutrients, effluent, and pollutants [21]. The mixing stirs the nutrient-rich Pacific water up into the surface layer, attracting a variety of plants and animals. As a result, Haro Strait is the home of killer whales and a lot of other marine wildlife. Studying tidal mixing also helps protect Haro Strait and similar environments. The Strait is a very busy shipping channel, along which numerous tankers carrying Alaskan oil. If a tanker ruptures in this area, emergency actions can be wisely taken only if we understand how waters in the Strait move and mix the spill [22].

Numerical models have been built for simulating currents in this region [23], [24]. Figure 2.2 shows the current flow field at flood tide at 23:03 (GMT) on June 28, 1996. However, direct measurements are severely lacking because the space and time scales of the tidal mixing process precludes satisfactory observations with traditional techniques [21]. Utilizing state-of-the-art technology, researchers from MIT and four other institutions led an expedition into Haro Strait in the summer of 1996 [3], [25]. Two Odyssey IIB AUVs were put into use. One of the vehicles was equipped with an ADCP, as shown in Figure 1.1. In this experiment, we were interested in making current velocity profiles, rather than making point measurement. Hence an ADCP was used instead of an Acoustic Doppler Velocimeter [26] which measures flow velocity at its acoustic focal location. On a mobile platform, the ADCP profiled current velocity, the key parameter characterizing the mixing process.

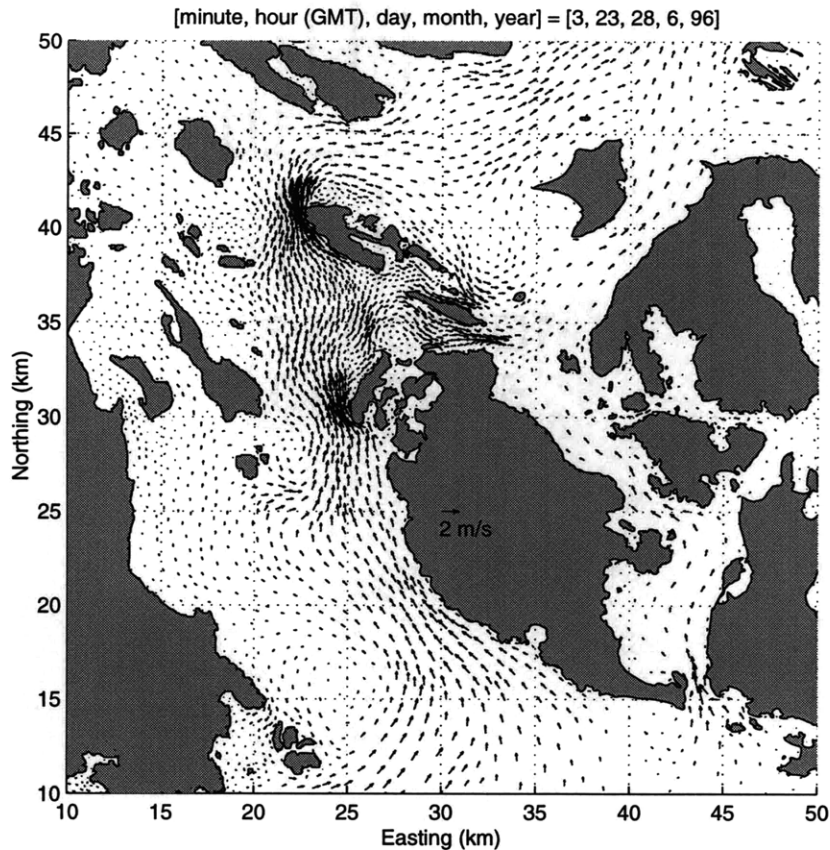


Figure 2.2: Flood flow at Haro Strait (using a tidal current model provided by Institute of Ocean Sciences, Canada).

2.2 Experimental Area and Grid Coordinate System

The experimental area was at the northern part of Haro Strait, to the south of Stuart Island which is labeled in Figure 2.1. Bathymetry of this area is shown in Figure 2.3. Intense mixing had been shown to occur in this area by ERS-1 Synthetic Aperture Radar images, aircraft photographs, and other means [21].

A set of projection parameters which are similar to those of Universal Transverse Mercator (UTM) were chosen to establish a convenient coordinate system for the Haro Strait region [3]. The WGS-84 ellipsoid was used along with the following specific projection parameters: central meridian 123°W (the same as UTM Zone 10) with false easting 40,000 m, latitude of origin $48^{\circ}30'\text{N}$ with false northing 20,000 m. The center

of projection is sufficiently close to the experimental area such that the distortion is negligible. In this scheme, the grid coordinates of the center of the experimental area are around northing 36,000 m by easting 24,000 m. The use of grid coordinates instead of geodetic ones greatly simplifies data processing.

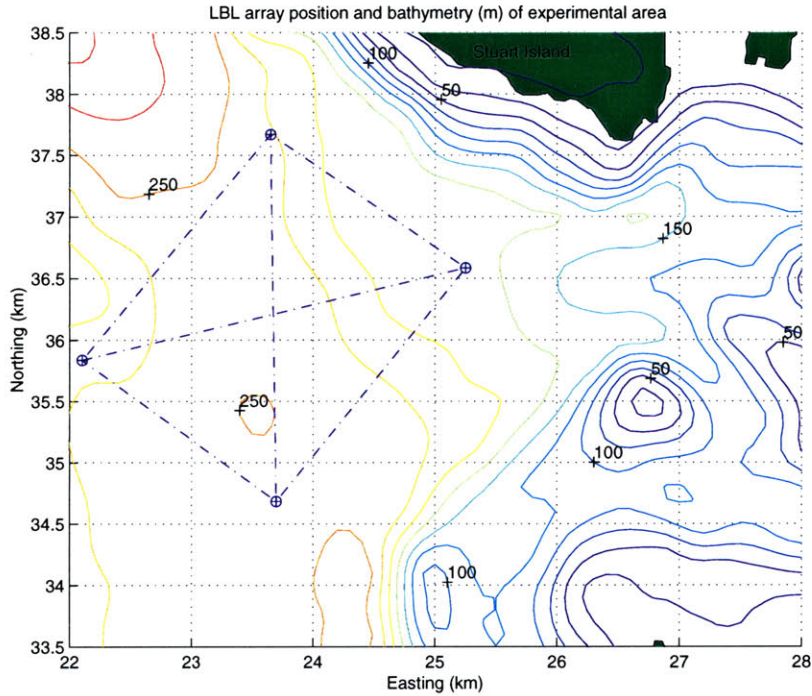


Figure 2.3: Grid coordinate system and bathymetry (in meter) of the experimental area. Four LBL acoustic transponders were deployed as marked by circles.

2.3 ADCP

An Workhorse ADCP [27] manufactured by RD Instruments (RDI) is selected to be used on an Odyssey IIB AUV. The RDI Workhorse ADCP is a four-beam system as shown in Figure 2.4, working at a frequency of 307.2 kHz with a wide bandwidth of about 75 kHz. Each of its four transducers both transmits acoustic pulses and receives reflections. The four acoustic beams point to four different directions, each with a slanting angle of 20° from the vertical axis of the ADCP unit. The Doppler principle applies only to the radial relative velocity, hence the current velocity is

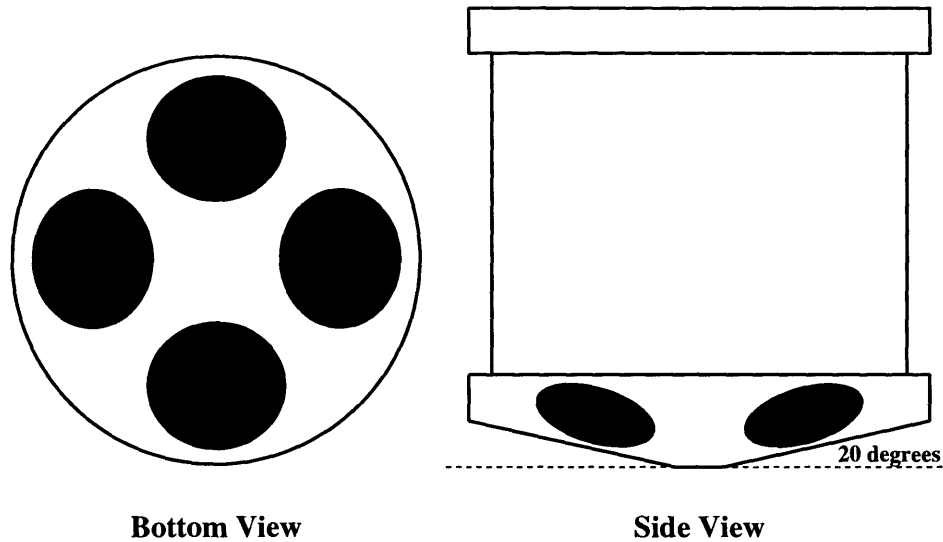


Figure 2.4: Bottom view and side view of the RDI ADCP unit.

originally measured as its projections along the four beam directions, called “beam velocity components”, as shown in Figure 2.5. With a compass and a pair of perpendicular tilt sensors inside the ADCP unit, it can transform the beam velocity into the East-North-Up (ENU) velocity in the Earth coordinate system. One pair of beam velocity components produces one horizontal component and the vertical component. The second pair produces the second, perpendicular horizontal component as well as the vertical component again. The “error velocity” is the difference between the two estimates of vertical velocity, which indicates the homogeneity within the same depth bin. At its working frequency, the ADCP’s profiling range is from 100 meters to 150 meters, depending on the specified depth bin size parameter. Using a broadband technique, the Workhorse ADCP features lower measurement noise than a narrow-band counterpart by a factor of about the square root of the bandwidth ratio [28]. The ratio is typically 100 for RDI ADCPs [4].

Ensemble period	No. of pings per ensemble	No. of depth bins	Depth bin size	Distance to 1st bin
2 s	1	50	2 m	4 m

Table 2.1: ADCP settings at Haro Strait.

Key parameters for setting the ADCP during the Haro Strait Experiment are listed

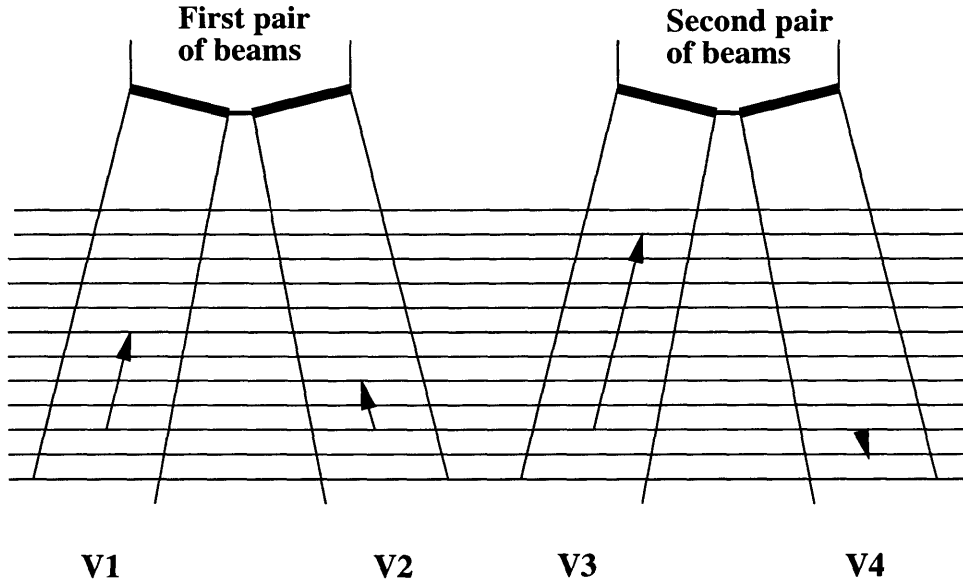


Figure 2.5: ADCP's four-beam radial velocity measurement over depth bins.

in Table 2.1. A “ping” refers to a short acoustic pulse transmitted by the ADCP. A velocity estimation error is associated with each single-ping measurement. Considering errors with individual pings uncorrelated, averaging reduces the overall error by the square root rule. The averaging is done on a group of pings, each group referred to as an “ensemble”. At Haro Strait, the tidal mixing process under survey from a rapidly moving platform featured high spatial variability. Consequently, reflected signals of different pings could in general come from considerably different water masses. Thus we chose to have only one ping per ensemble. Based on the bathymetry of the experimental area, the ADCP was designated to make profiles of 100 m depth range which was divided into 50 bins each of 2 m size. Given the above parameters, the ADCP's transmission time plus the overhead processing time determines that the ensemble interval is 2 s. Ensemble cycling and ping cycling were both set to be automatic. The ADCP needs time to switch from the transmission mode to the reception mode. Therefore, it blanks out reflections close to the transducer head. The distance of the first bin from the ADCP was 4 m in the Haro Strait settings. Current velocity data presented in the thesis were recorded in the East-North-Up (ENU) coordinate system with transformation work already done by ADCP's internal processing. Transformation from the ADCP's local forward-sideway-up coordinate system to the

ENU coordinate system is carried out using the ADCP's internal heading/pitch/roll sensors.

As explained in Chapter 1, current velocity is averaged within the same depth bin to give the reading. Larger depth bin size implies more averaging within the same bin and hence lower velocity measurement noise, under the assumption of laterally homogeneous current velocity within the same bin. Coarser depth segmentation, on the other hand, means worse vertical resolution. Thus there is a trade-off between measurement noise and vertical resolution. At Haro Strait, the depth bin size was set to 2 m. Under this setting, the ADCP's single-ping velocity measurement noise is 7.0 cm/s for horizontal and 3.6 cm/s for vertical.

The ADCP was powered by the vehicle's battery pack. Its communications with the vehicle's computer were through an RS-232 port. The ADCP's raw data were in binary format and recorded in its internal memory of 10 MB space. With the settings outlined in Table 2.1, 20-minute data logging requires about 1 MB. At Haro Strait, a typical mission day was less than 200 minutes, so the ADCP's memory space was enough to hold data of the whole day. At the end of the day, the data were downloaded onto an outside PC via an external RS-232 cable. Control of the ADCP was only partially integrated with the vehicle software at the time of the Haro Strait Experiment, requiring the ADCP be awakened by a manual command during the pre-launch countdown of a mission. All controls for ADCP have since been incorporated into the main vehicle software. Time synchronization will be elaborated in Section 3.1.1.

2.4 Long-BaseLine (LBL) Navigation Array

A Long-BaseLine (LBL) acoustic transponder array provided the externally referenced navigation for the AUV [3]. Four transponders were deployed in a slightly skewed parallelogram with side lengths of about 2 km and 2.5 km, as shown in Figure 2.3. Frequencies used were in the 8.5 ~ 13 kHz range. The navigation principle of an LBL system is as follows. During an AUV run, the vehicle's transceiver broadcasts acoustic

pulses to all transponders. On reception, the transponders send response signals using distinct frequencies. The AUV's transceiver receives the responses, and calculates the acoustic travel time for each transponder. As locations of the transponders are known, the vehicle's position is obtained based on acoustic travel times and sound speed which is derived from CTD casts. Calibration of LBL transponder locations was performed from the ship utilizing Differential GPS (DGPS).

LBL positioning error sources include watch-circle of the moored transponders, error of array calibration, errors due to incorrect modeling of water properties, and time jitter of acoustic pulse detection. In addition, depth measurement offset is also an error source, as will be pointed out in Section 2.5. Calculated by Dr. Bradley Moran [3], the positioning accuracy of the Haro Strait LBL system is better than 10 m and the precision is better than 2 m, when the vehicle's distance from the array center is less than the array aperture.

2.5 AUV's Depth Measurement

The vehicle's depth sensor used in the Haro Strait Experiment was Paroscientific Model 8B-4000. It has an accuracy of 0.4 m [29], and its precision is much better than 0.2 m.

Elevation of the water surface varies with tide in the experiment area. Water level at the time of LBL array calibration could be different from that at the time of an AUV mission. Under such a circumstance, the zero-depth reference used for the vehicle's depth measurement differs from that used by the LBL array calibration record. The resultant depth offset for the transponders translates into LBL ranging errors.

2.6 Heading/Pitch/Roll Measurements of AUV and ADCP

The vehicle uses KVH digital gyro compass and inclinometer for its heading/pitch/roll measurements [30]. The ADCP uses its internal heading/pitch/roll sensors for conducting coordinate transformation for velocity measurement.

	heading	pitch / roll
KVH	$\pm 0.5^\circ$	$\pm 1^\circ$
ADCP	$\pm 1^\circ$	$\pm 2^\circ$

Table 2.2: Heading/pitch/roll sensors' accuracy (at tilt angles up to $\pm 20^\circ$) comparison.

AUV's KVH sensors are twice as accurate as those of ADCP's, as compared in Table 2.2, based on manufacturers' specifications. The performance difference shown in experiments is probably even greater. It is also found that at Haro Strait the ADCP's compass gave considerable bias at some headings, possibly affected by the AUV battery's magnetic field due to the ADCP's proximity to the vehicle's battery sphere. As a result, correction is made on ADCP's velocity measurement, using KVH's readings as better references. For the two reciprocal legs during Mission 14 on June 25 (as shown in Figure 3.7), current velocity estimates using corrected ADCP data are much more consistent than using raw data. The correction procedure will be elaborated in Chapter 3. At the time of the Haro Strait Experiment, the magnetic variation in the region was 18.9° . This variation is taken care of in data processing.

Chapter 3

Data Post-Processing Method

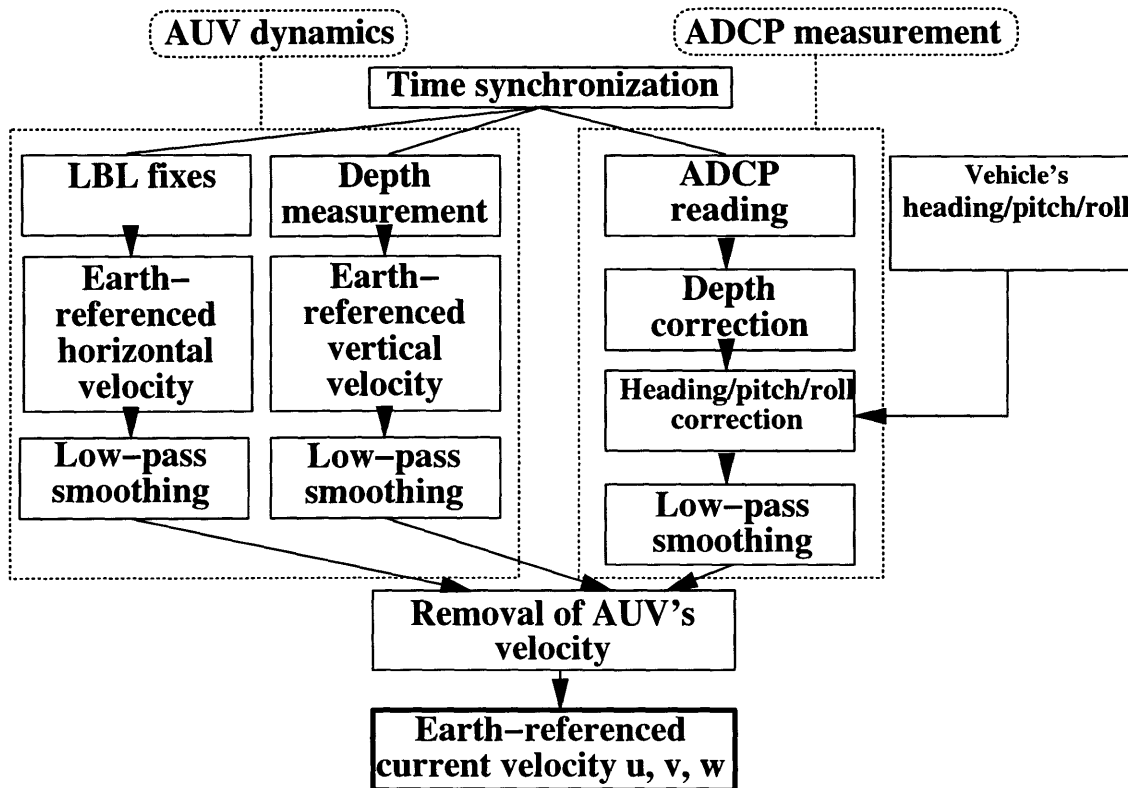


Figure 3.1: Block diagram of the data post-processing procedure.

The data processing procedure is summarized in Figure 3.1. The central point is to remove the AUV's velocity from the ADCP's raw measurement. Individual computation components are described in Section 3.1, and results are presented in Section 3.2.

3.1 Data Processing Method

3.1.1 Time Synchronization

A common time reference must be set up before merging data from different sensors. During the Haro Strait Experiment, LBL data and AUV-borne CTD data were stamped with the vehicle's time which was set to the GPS time once every day. The ADCP had a separate clock which was manually set before each mission. The approximate one-second error of ADCP clock is compensated in data post-processing by careful alignment of heading/pitch/roll measurements made by the vehicle and by the ADCP. In this way, LBL data and vehicle CTD data are synchronized with ADCP data on the common GPS time reference. Subsequent to the Haro Strait Experiment, synchronization has been automated.

3.1.2 Estimating AUV's Own Velocity

1. Horizontal velocity.

The bottom-track function was not equipped with the RDI Workhorse ADCP at the time of the Experiment. As a result, the LBL navigation record is used for estimating the vehicle's horizontal position. Differentiation of sequential positions gives the AUV's horizontal velocity.

2. Vertical velocity.

The AUV's Vertical velocity is estimated by differentiating its on-board depth sensor measurements.

3. Error Sources. To reduce the overall noise of current velocity estimates, low-pass smoothing is conducted as will be discussed in Section 3.1.5.

3.1.3 Sources of Errors

1. LBL fixes. As mentioned in Section 2.4, the positioning precision is 2 m. Note that in estimating the vehicle's own velocity, differentiation is done on adjacent

position data. Hence positioning precision, rather than accuracy, is used for getting the velocity estimation uncertainty. The time interval between adjacent LBL fixes is 10 s.

2. AUV's Depth measurement. As mentioned in Section 2.5, the depth precision is much better than 0.2 m, taken as $(0.2 \text{ m}) \times 0.3 = 0.06 \text{ m}$. The time interval between adjacent depth measurements is 0.2 s. Elevation of the water surface varies with tide. As pointed out in Section 2.5, the possibly different zero-depth references used by the vehicle and by the array calibration record may slightly contribute to the errors in LBL fixes.
3. ADCP measurement. As mentioned in Section 2.3, Under its settings for the Haro Strait Experiment, the ADCP's single-ping velocity measurement noise is 7.0 cm/s for horizontal and 3.6 cm/s for vertical. Correction of errors resulting from ADCP's inaccurate heading/pitch/roll measurements will be discussed in Section 3.1.4.

In the ADCP's calculations, it is assumed that water current velocity is homogeneous in the same depth bin over the span of its slanted acoustic beams. When there is considerable horizontal spatial variation of current velocity, the above assumption may not hold satisfactorily, especially for greater ranges as slanted beams span wider. This shortcoming is intrinsic to the ADCP's working principle.

4. Attitude-related variation of ADCP measurement. During a yo-yo mission as depicted by Figure 3.2, the ADCP's acoustic beams sharply pitch up or down at the vertical turning points. For upper turning points and lower turning points, horizontal locations of the ensonified water columns relative to the vehicle are different. The resultant effects are ignored in this thesis since low-pass smoothing is later applied.

3.1.4 Corrections of ADCP Measurement

1. Depth correction.

During an AUV mission, especially a yo-yo mission, the vehicle's depth varies. The depth bin numbering of ADCP data is from the vehicle, as illustrated in Figure 3.2. Therefore, correction is done such that depth is in the absolute sense (i.e., relative to the water surface) in the final current velocity profile. Figure 3.2 describes a yo-yo mission of the AUV, with ADCP's depth bin numbers labeled. The final current velocity profile is made on the shaded rectangular section.

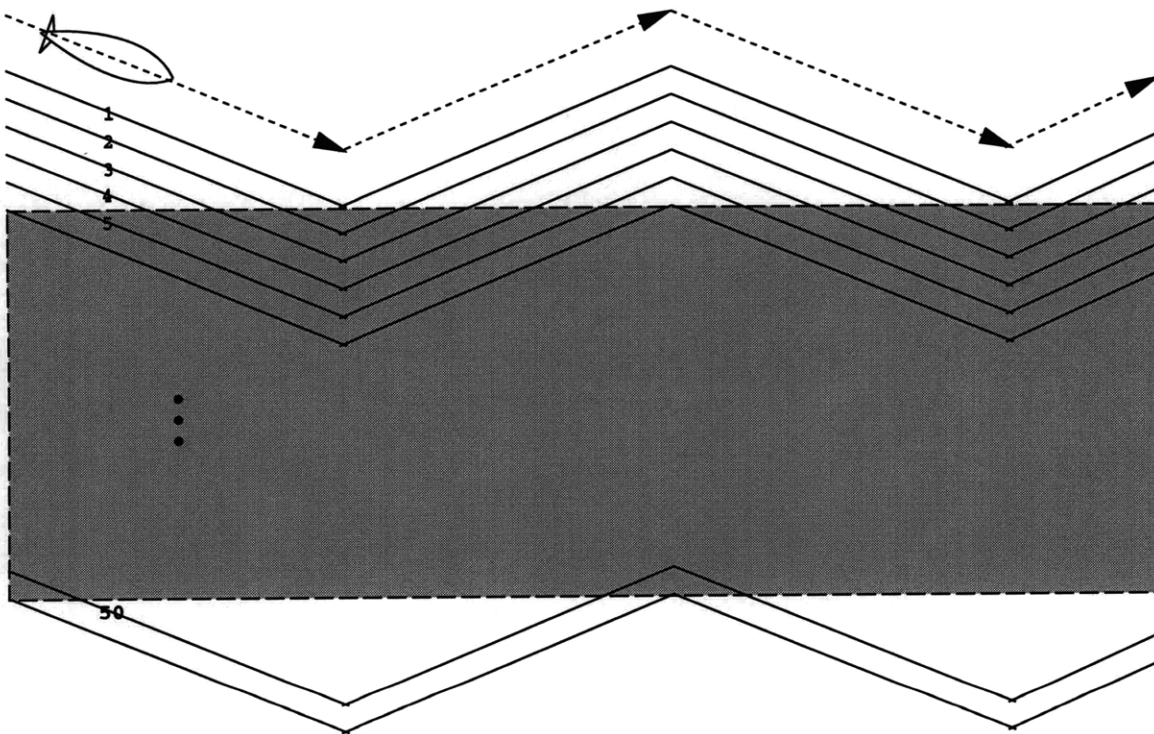


Figure 3.2: Depth bin numbering correction for ADCP data.

2. ENU transformation correction.

As pointed out in Section 2.6, accuracy of the AUV's KVH heading/pitch/roll sensors is twice as high as that of the ADCP's internal sensors. The ADCP's current velocity data presented in the thesis were recorded in the East-North-Up (ENU) coordinate system. Transformation from the ADCP's local forward-

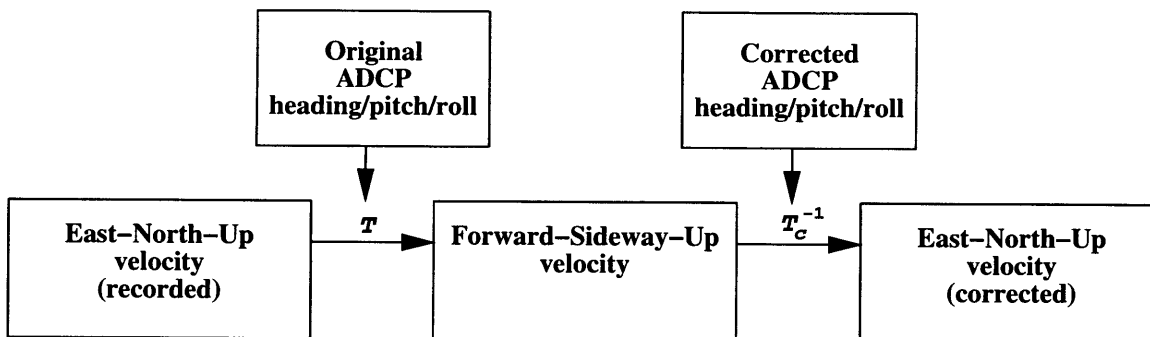


Figure 3.3: ENU transformation correction for ADCP velocity.

sideway-up coordinate system to the ENU coordinate system was carried out on-site by the ADCP using its internal heading/pitch/roll sensors. For better data quality, heading/pitch/roll used in ADCP’s internal transformation are corrected by using the vehicle’s KVH measurements as better references. The corrected values are then used in calculating the corrected ENU velocity. The diagram is shown in Figure 3.3. The correction procedure is as follows.

- (a) Transform velocity from the ENU coordinate system back to the ADCP’s local forward-sideway-up coordinate system. Transformations in both directions are based on the successive rotations illustrated in Figure 3.4.

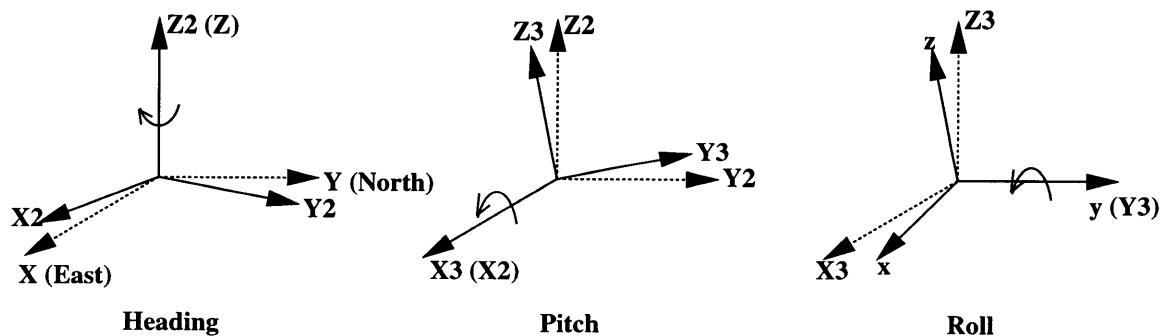


Figure 3.4: Rotations by heading, pitch, and roll.

The transformation from ENU coordinate system $X - Y - Z$ to local forward-sideway-up coordinate system $x - y - z$ can be implemented by three successive rotations: heading, pitch, and roll, as expressed by the

following equations.

$$\text{Heading } \theta_h : \begin{bmatrix} X2 \\ Y2 \\ Z2 \end{bmatrix} = \begin{bmatrix} \cos(\theta_h) & -\sin(\theta_h) & 0 \\ \sin(\theta_h) & \cos(\theta_h) & 0 \\ 0 & 0 & 1 \end{bmatrix} \begin{bmatrix} X \\ Y \\ Z \end{bmatrix} = A \begin{bmatrix} X \\ Y \\ Z \end{bmatrix} \quad (3.1)$$

$$\text{Pitch } \theta_p : \begin{bmatrix} X3 \\ Y3 \\ Z3 \end{bmatrix} = \begin{bmatrix} 1 & 0 & 0 \\ 0 & \cos(\theta_p) & \sin(\theta_p) \\ 0 & -\sin(\theta_p) & \cos(\theta_p) \end{bmatrix} \begin{bmatrix} X2 \\ Y2 \\ Z2 \end{bmatrix} = B \begin{bmatrix} X2 \\ Y2 \\ Z2 \end{bmatrix} \quad (3.2)$$

$$\text{Roll } \theta_r : \begin{bmatrix} x \\ y \\ z \end{bmatrix} = \begin{bmatrix} \cos(\theta'_r) & 0 & -\sin(\theta'_r) \\ 0 & 1 & 0 \\ \sin(\theta'_r) & 0 & \cos(\theta'_r) \end{bmatrix} \begin{bmatrix} X3 \\ Y3 \\ Z3 \end{bmatrix} = C \begin{bmatrix} X3 \\ Y3 \\ Z3 \end{bmatrix} \quad (3.3)$$

where matrices A , B , and C represent the three rotation matrices, respectively.

Note that there is a subtlety in the roll rotation. The measured roll angle is referenced to the horizontal plane, rather than a rotation about the y-axis. Trigonometric derivation gives the relation between the desired rotation angle θ'_r and the roll measurement θ_r as expressed by Equation (3.4). When pitch angle θ_p is small, the difference between θ_r and θ'_r is small too.

$$\theta'_r = \text{acos}\left(\frac{\cos(2\theta_r) + \cos(2\theta_p)}{2\cos(\theta_p)\sqrt{\cos^2(\theta_p) - \sin^2(\theta_r)}}\right) \times \text{sign}(\theta_r) \quad (3.4)$$

Therefore, v_x , v_y , and v_z in the ADCP's local forward-sideway-up coordinate system are related with v_X , v_Y , and v_Z in the ENU coordinate system by the following equation:

$$\begin{bmatrix} v_x \\ v_y \\ v_z \end{bmatrix} = (CBA) \begin{bmatrix} v_X \\ v_Y \\ v_Z \end{bmatrix} \quad (3.5)$$

- (b) Then, θ_h , θ_p , and θ_r measured by the ADCP's internal sensors are corrected using the AUV's KVH sensors. The corrected heading, pitch, and roll angles are θ_{hc} , θ_{pc} , and θ_{rc} , respectively. ENU current velocity measured by the ADCP is accordingly corrected using θ_{hc} , θ_{pc} , and θ_{rc} , resulting in v_{Xc} , v_{Yc} , and v_{Zc} :

$$\begin{bmatrix} v_{Xc} \\ v_{Yc} \\ v_{Zc} \end{bmatrix} = (C_c B_c A_c)^{-1} \begin{bmatrix} v_x \\ v_y \\ v_z \end{bmatrix} = (C_c B_c A_c)^{-1} (CBA) \begin{bmatrix} v_X \\ v_Y \\ v_Z \end{bmatrix} \quad (3.6)$$

where matrices A_c , B_c , and C_c are the same as A , B , and C in Equation (3.1), Equation (3.2), and Equation (3.3), except that θ_{hc} , θ_{pc} , and θ_{rc} replace θ_h , θ_p , and θ_r , respectively.

- (c) θ_{hc} , θ_{pc} , and θ_{rc} are derived from the AUV's KVH measurements. The mounting orientation of the ADCP makes the calculations not straightforward. The ADCP's mounting plane is parallel to that of the KVH box. Hence for trigonometric calculations, the two pairs of pitch/roll axes can be deemed lying in the same plane. The relation between the two sets of pitch/roll angles is illustrated in Figure 3.5.

$\alpha = 45^\circ$ is the mounting angle between the ADCP's forward direction and the AUV's bow direction. γ is the projection of α on the horizontal plane. Pitch θ_1 and roll θ_2 are KVH measurements. Corrected pitch θ_{pc} and corrected roll θ_{rc} of the ADCP are derived from θ_1 and θ_2 , based on

the mounting constraint of the ADCP. Thus corrected pitch and roll for the ADCP are obtained as follows:

$$\theta_{pc} = -asin[(sin(\theta_2) - sin(\theta_1)cot(\alpha))sin(\alpha)] \quad (3.7)$$

$$\theta_{rc} = asin[(sin(\theta_2) + sin(\theta_1)tan(\alpha))cos(\alpha)] \quad (3.8)$$

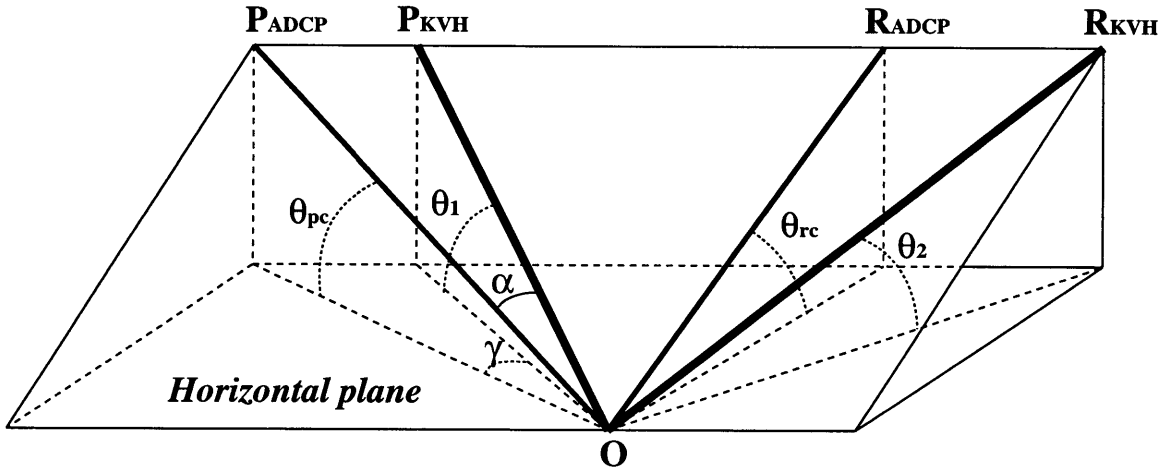


Figure 3.5: Pitch/roll for ADCP's internal sensors and AUV's KVH sensors.

The relation between headings measured by the ADCP and the AUV's KVH is illustrated in Figure 3.6. Note that KVH-measured heading is of the vehicle bow's projection on the horizontal plane, while the ADCP-measured heading is of its forward's projection. As first noted in Figure 3.5, γ is the projection of mounting angle $\alpha = 45^\circ$ on the horizontal plane.

It can be shown that

$$\gamma = acos\left[\frac{cos(\alpha)}{cos(\theta_1)cos(\theta_{pc})} - tan(\theta_1)tan(\theta_{pc})\right] \quad (3.9)$$

where θ_{pc} is expressed by Equation (3.7).

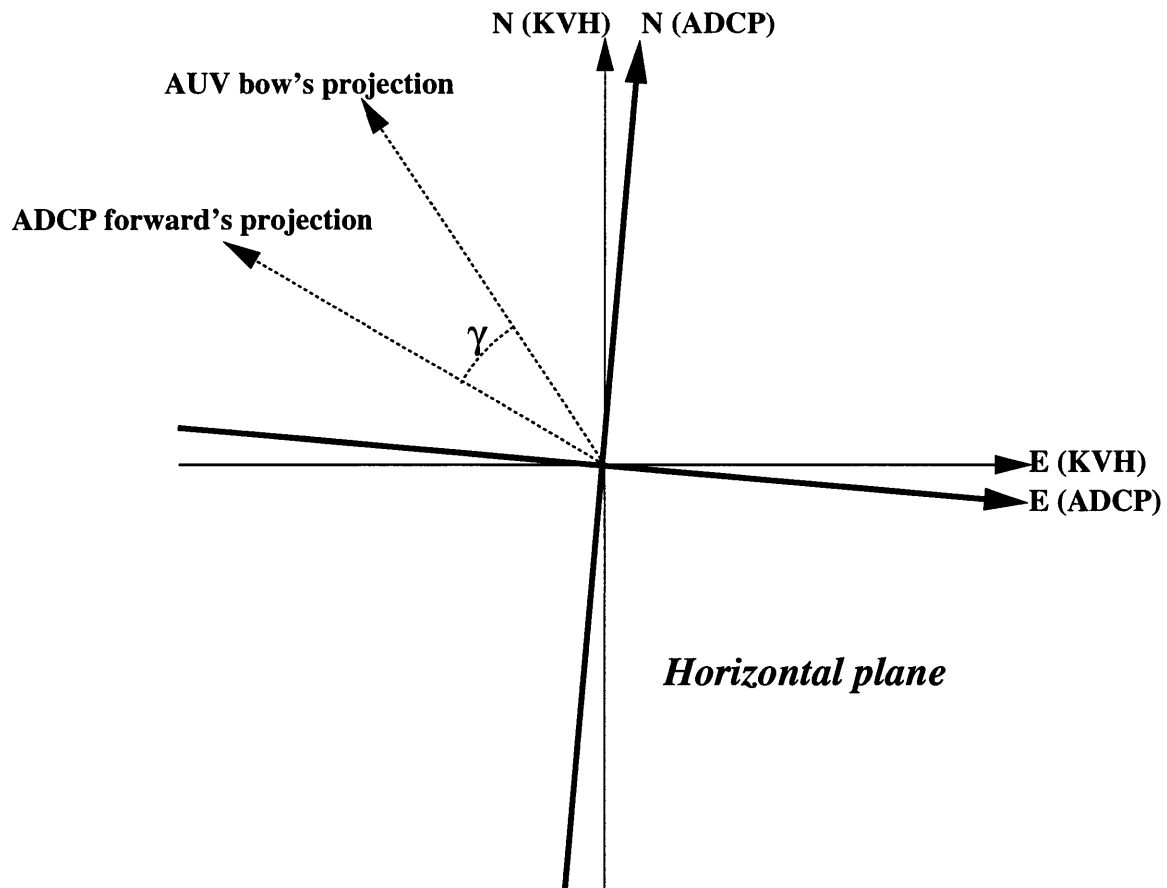


Figure 3.6: Headings measured by ADCP's internal compass and AUV's KVH compass.

We rectify ADCP-measured heading using KVH's North/East as the correct reference:

$$\theta_{hc} = \theta_{hKVH} - \gamma \quad (3.10)$$

where θ_{hc} is the corrected value of the ADCP-measured heading, and θ_{hKVH} is the KVH-measured heading. γ is expressed by Equation (3.9).

Using Equation (3.7), Equation (3.8), and Equation (3.10), heading, pitch, and roll measured by ADCP are corrected. The corrected values are used in Equation (3.6) to obtain corrected current velocity in the ENU coordi-

nate system.

3.1.5 Low-Pass Smoothing

Single-ping measurement noise of the raw ADCP current velocity data, as noted in Section 2.3, is unsatisfactorily large compared with the true current velocity. The problem of measurement noise is more severe with estimate of the AUV's horizontal velocity based on LBL navigation data, because the positioning precision 2 m translates into a large velocity uncertainty in the process of differentiation. A similar problem is associated with estimating the vehicle's vertical velocity by differentiating its depth measurements.

A rectangular moving-average window is applied to ADCP measurements, and estimates of vehicle's own velocity. The longer the window, the smaller the output noise, but the worse the temporal resolution. Temporal resolution can be translated into spatial resolution, given the vehicle's cruising speed. Therefore, there is a trade-off between temporal (spatial) resolution and noise reduction. The rule of thumb used in the thesis is to make the smoothing window just long enough to suppress the velocity noise to being around 10% of the true current velocity magnitude.

3.1.6 Extraction of Earth-Referenced Current Velocity

As the final step, the AUV's own velocity is removed from the relative current velocity measured by the ADCP. The remnant is the Earth-referenced current velocity we are looking for.

3.2 Data Processing Results

Current velocity results for two typical AUV missions of the Haro Strait Experiment are presented in this section.

1. Mission 14 on June 25, 1996.

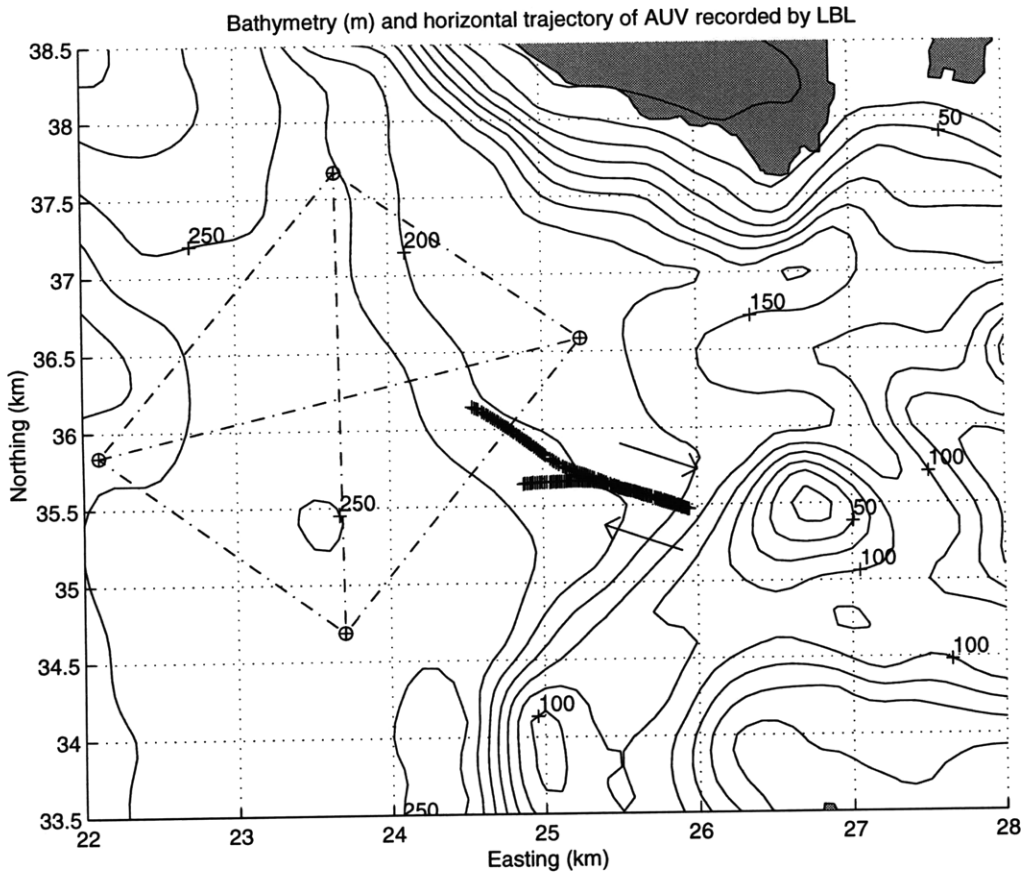


Figure 3.7: Horizontal trajectory of the AUV during Mission 14 on June 25, 1996.

During this mission, the vehicle yo-yo’ed between the surface and a depth of 20 m. The vehicle’s horizontal and vertical trajectories are shown in Figure 3.7 and Figure 3.8, respectively. Its commanded heading was 108.9° (True) for 1200 s and then a reciprocal course of 288.9° (True) for 900 s, as shown by the arrows in Figure 3.7. The discrepancy between the AUV’s dead-reckoned track and the actual track affected by the current will be discussed shortly. The vehicle’s horizontal speed was about 1.3 m/s.

Raw ADCP measurements are shown in Figure 3.9. The vehicle’s $\sim 30^\circ$ pitch angle in this yo-yo mission made the ADCP’s acoustic beams be slanted against the vertical direction. The ADCP’s effective vertical range, which is the pro-

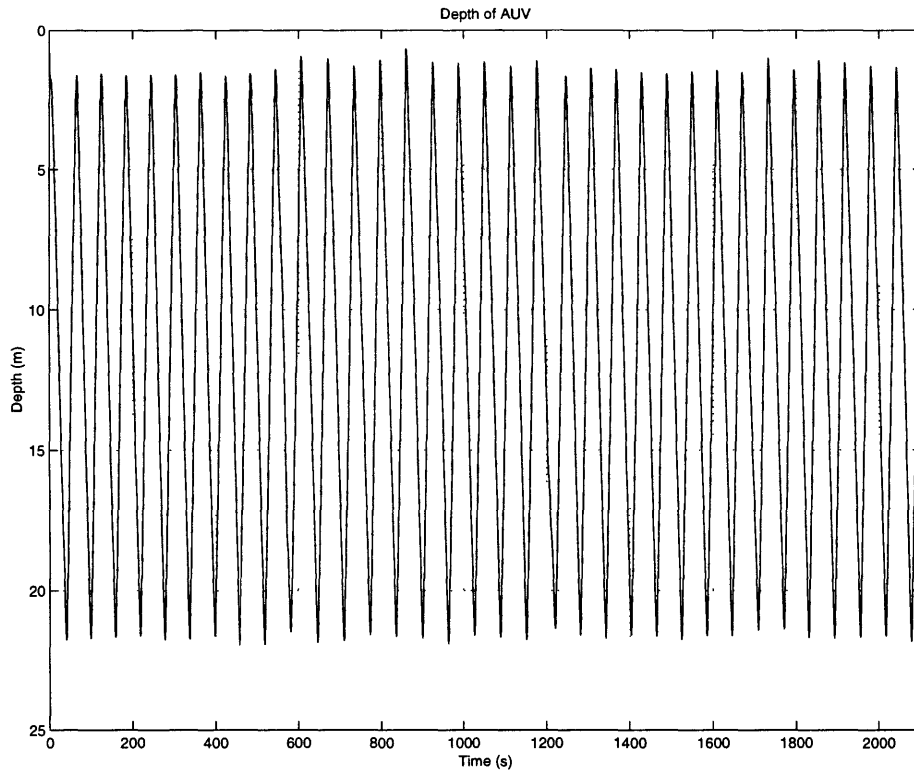


Figure 3.8: Vertical trajectory of the AUV during Mission 14 on June 25, 1996.

jection of its radial range on the vertical axis, was consequently decreased. It turns out that only 40 out of the total 50 bins have good data. When the AUV runs at a nearly constant depth without significant pitch, this shortcoming does not show up.

As discussed in Section 3.1.4, depth correction is carried out to counteract the large depth variation. A profile is made over a rectangular vertical section with depth bounds of 26 m and 82 m. It should be noted that the vehicle's yo-yo mission introduced a substantial vertical velocity anomaly, which is obvious in the third panel of Figure 3.9.

Using the data processing method presented in Section 3.1, the Earth-referenced current velocity is obtained, as shown in Figure 3.10. Within the studied depth range, the water flowed mostly southward with a maximum velocity of about

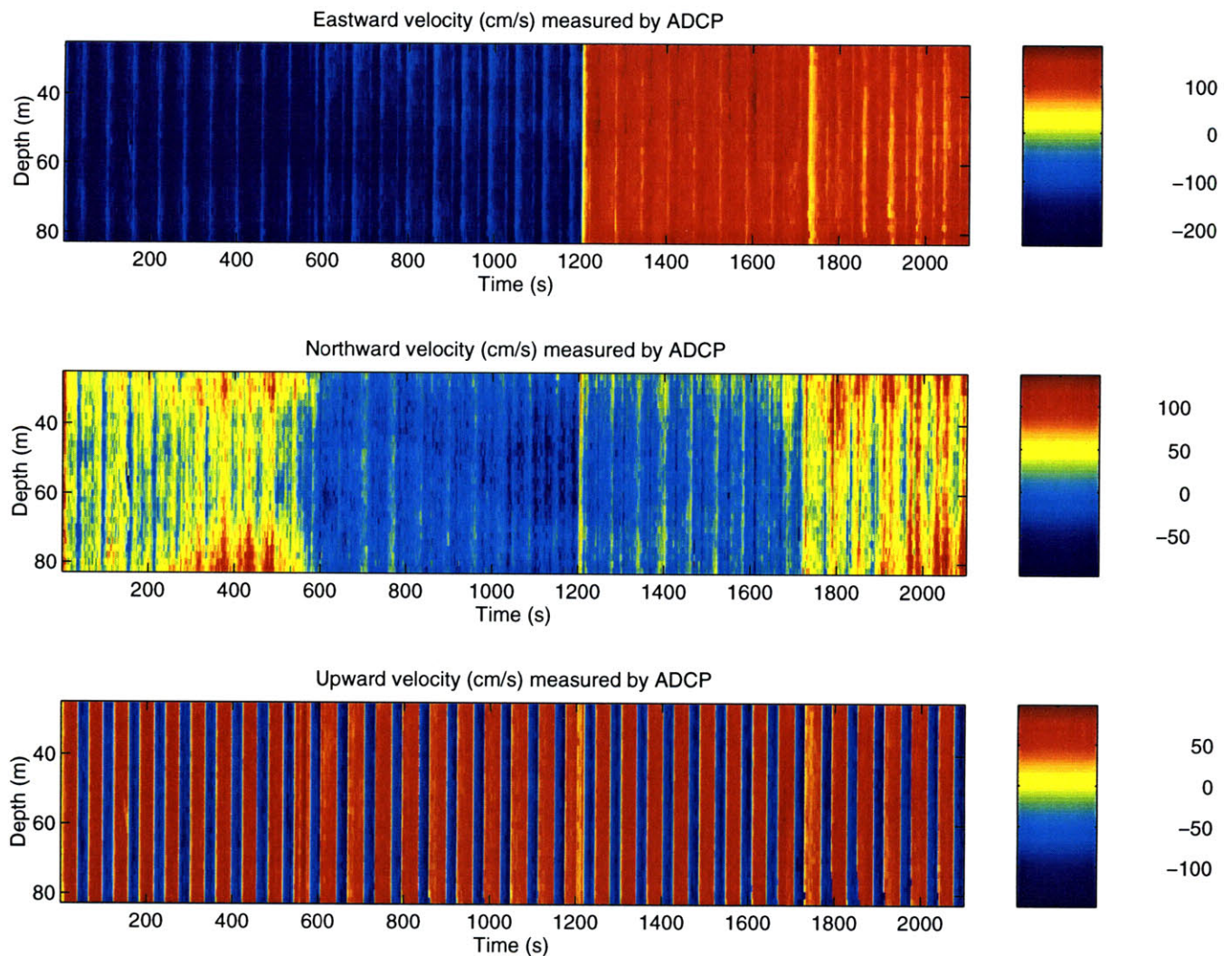


Figure 3.9: Raw current velocity measured by the ADCP during Mission 14 on June 25, 1996.

40 cm/s. Eastward velocity demonstrates a shear structure: the water above 40-meter depth flowed to the east at about 10 cm/s while the water below flowed to the west with velocity up to 30 cm/s. This shear current structure reveals the layered feature of the tidal mixing process. In the vertical direction, alternating upwellings and downwellings were of velocity up to 10 cm/s. The dominating signature of the vehicle's own vertical motion as shown in Figure 3.9 has been mostly removed.

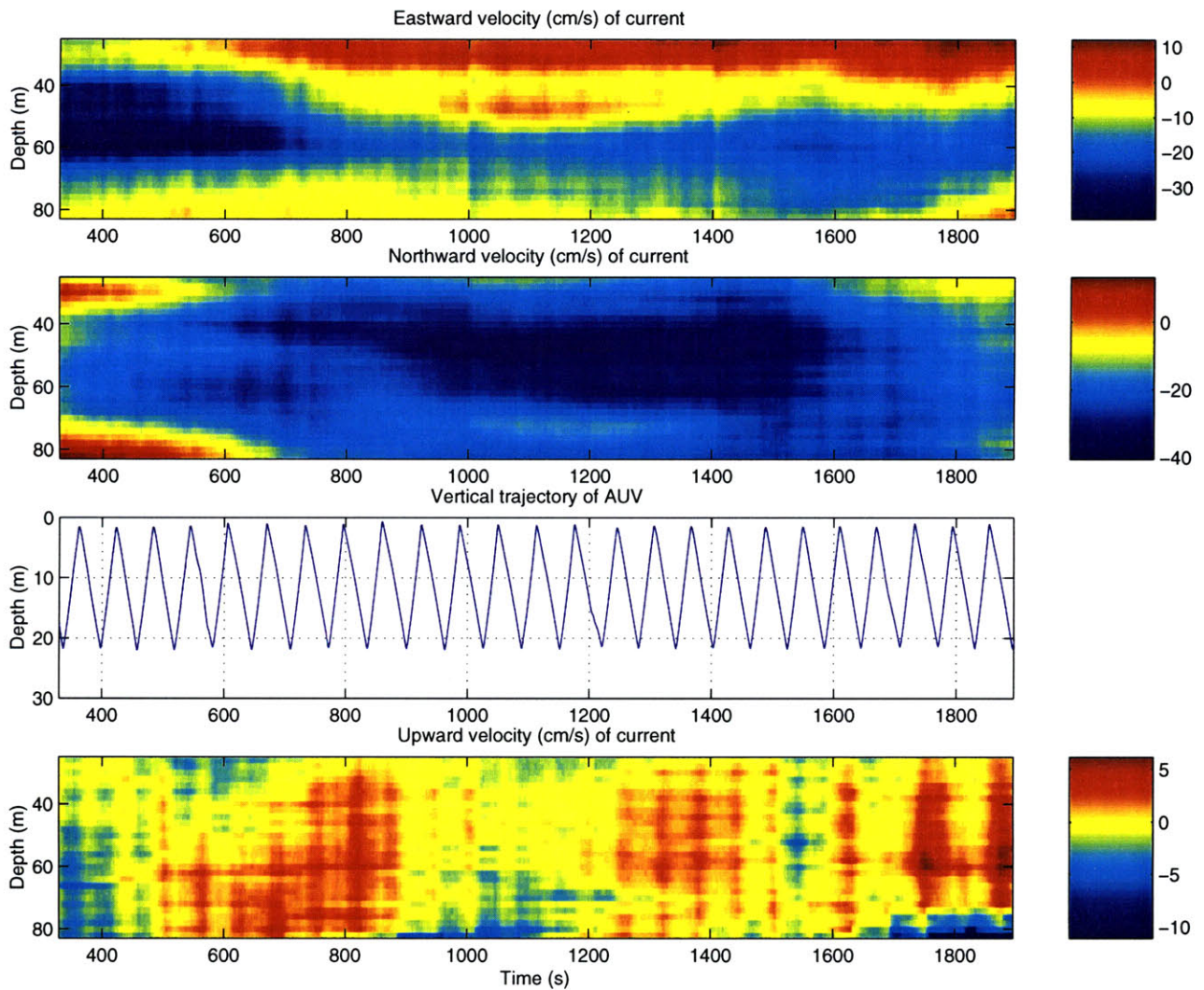


Figure 3.10: Computation result of Earth-referenced current velocity for Mission 14 on June 25, 1996.

To reduce current velocity estimation errors to acceptable levels, 400-second smoothing and 200-second smoothing are done on the horizontal velocity and the vertical velocity, respectively. After smoothing, the root-mean-square (rms) error of Earth-referenced horizontal current velocity is about 3 cm/s, while the velocity magnitude is as large as 30 cm/s. One may notice two minor discontinuities of eastward velocity at around 1000 s and 1400 s. They are caused by the direction reversal of the vehicle at around 1200 s. In post-processing, when either edge of the 400-second smoothing window slides past this instant, a big change of new velocity values will affect the smoothing output. Errors in

estimating vertical current velocity are smaller than those in estimating horizontal current velocity, so the applied smoothing window is shorter for vertical current velocity estimation. After smoothing, the rms error of Earth-referenced vertical current velocity is about 1 cm/s while the velocity magnitude is as large as 10 cm/s. It should be noted that the LBL navigation error is the dominant error source in extracting horizontal current velocity. This necessitates a long smoothing window. Therefore we cannot overemphasize the importance of good navigation. Later work on the LBL system has shown very promising results in a series of trials that took place at Cape Cod Bay in May 1997.

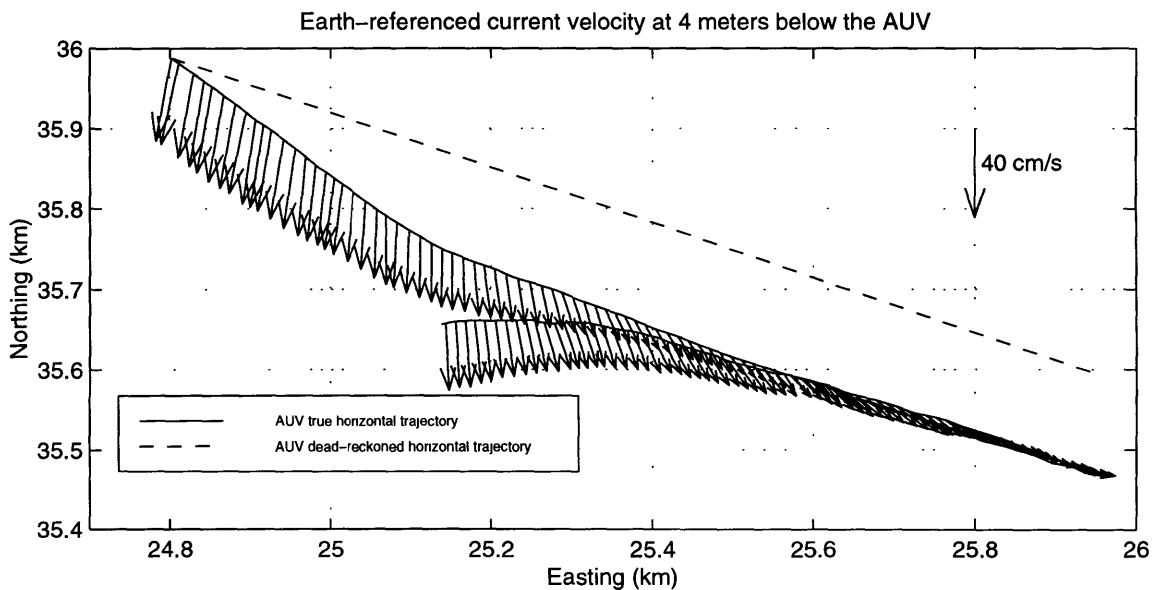


Figure 3.11: Horizontal current velocity near the AUV and its effect on the AUV's trajectory during Mission 14 on June 25, 1996.

Figure 3.11 shows the Earth-referenced horizontal current velocity in the vicinity of the AUV. It is based on current velocity measurements in the first depth bin which was 4 m below the vehicle. These measurements were made so close

to the AUV that they are considered to represent the water current that applied hydrodynamic forces on the vehicle. Note that only one velocity data point out of every five is used in Figure 3.11 to ensure that the arrows are not too crowded. Near the vehicle, there existed significant southward current up to about 40 cm/s in the west segment of the vehicle's track. This southward current weakened toward the east segment. The current velocity near the AUV had an apparent effect on the vehicle's trajectory. As originally commanded, the vehicle's dead-reckoned horizontal trajectory is: 108.9° heading for 1200 s and then a reciprocal course of 288.9° heading for 900 s, shown by the dashed line in Figure 3.11. The vehicle's actual trajectory, shown by the solid line, is obviously flushed southward, under considerable hydrodynamic forces.

In Figure 3.12, vertical current velocity, AUV-measured depth, temperature, and salinity are displayed on the same time reference. At around 600 s, the vehicle crossed a front, entering a lower-temperature and higher-salinity water mass. Then at around 1200 s, the vehicle turned around. At around 1700 s, it crossed the front again in the reverse direction, and returned to the higher-temperature and lower-salinity water. Current velocity combined with CTD data is useful for a better understanding of the studied process.

2. Mission 11 on June 28, 1996.

During this mission, the AUV was commanded to run at a constant depth of about 10 m. The results here only show part of the mission which was the last southeastward leg of this way-point mission. Afterwards the vehicle flew very close to Danger Shoal with a bathymetry shallower than 25 m. The vehicle's horizontal and vertical trajectories are shown in Figure 3.13 and Figure 3.14, respectively.

Raw ADCP measurements are shown in Figure 3.15. All of the 50 depth bins produced good data. Depth correction leads to a profile over a rectangular ver-

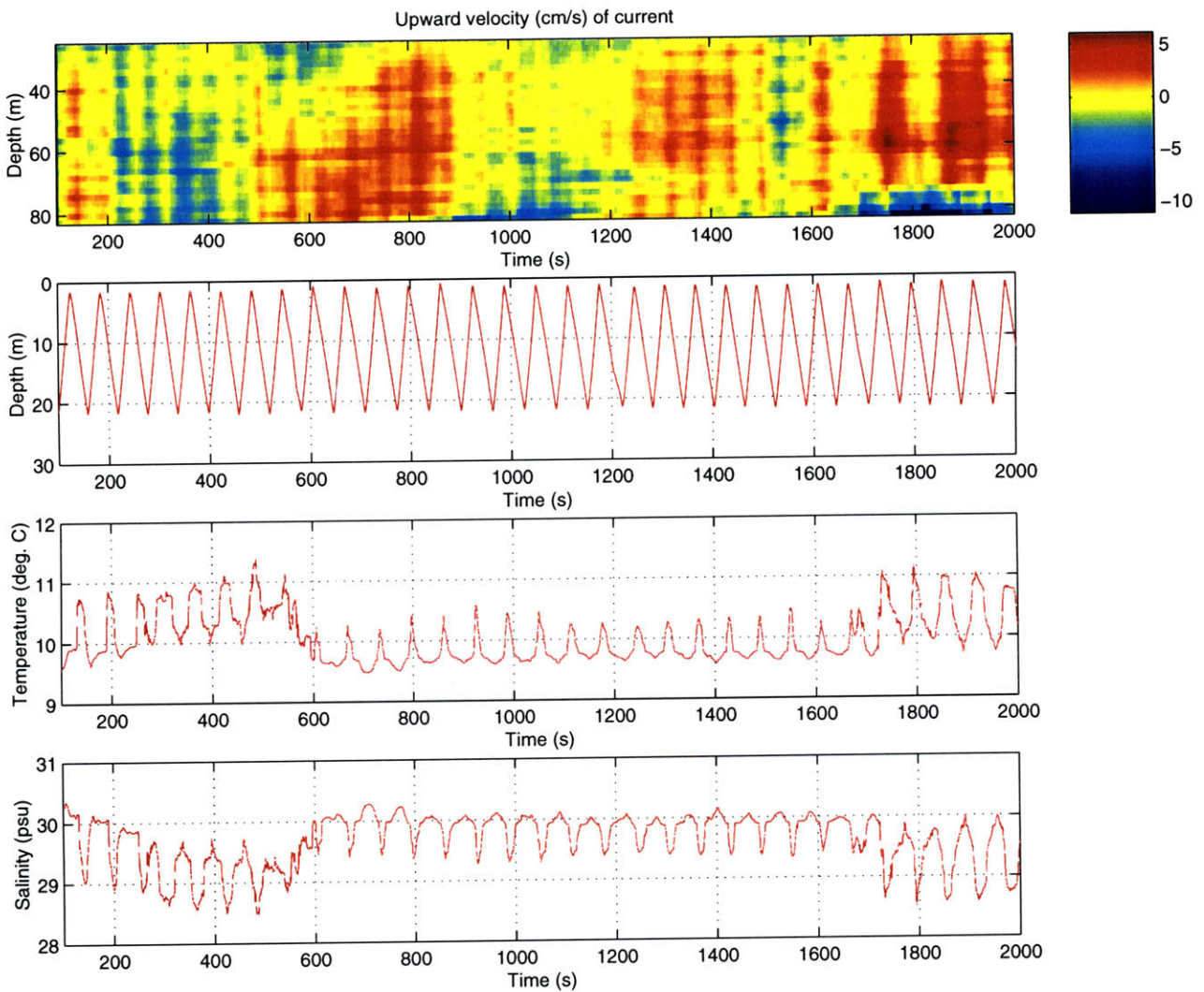


Figure 3.12: Vertical current velocity along with AUV's CTD measurements during Mission 14 on June 25, 1996.

tical section with depth bounds of 16 m and 102 m.

Earth-referenced current velocity between depths of 16 m and 102 m are shown in Figure 3.16. Shear structure of horizontal current flow appears again. Before around 900 s, the current was southward above 40-meter depth, but the current was northward below this depth. It is interesting to compare this result with the tidal current model result at the time of this mission which is shown in Figure 2.2. The mission took place at flood tide. The shear structure of horizontal current velocity is an indication of deeper sea water flooding in while surface

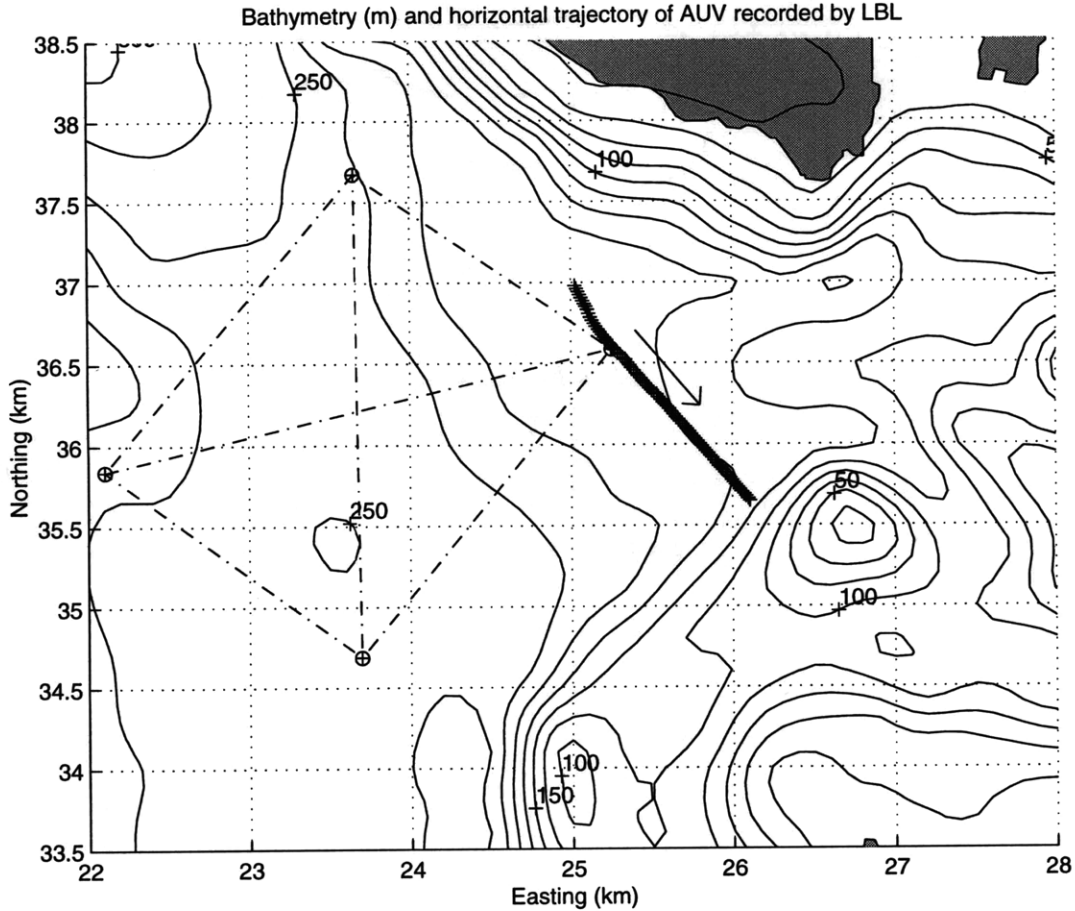


Figure 3.13: Horizontal trajectory of the AUV during Mission 11 on June 28, 1996.

fresh water flushed out. This observation is important for understanding the tidal mixing process.

Upwellings of up to 10 cm/s are seen in the beginning (west) segment of the mission. Owing to the higher magnitude of both horizontal current velocity (~ 40 cm/s) and vertical current velocity (~ 10 cm/s) than those in Mission 14 on June 25, shorter smoothing windows are used. For the horizontal velocity, a 200-second smoothing window is applied, giving an rms error of about 5 cm/s. For the vertical velocity, an 100-second smoothing window is applied, giving an rms error of about 1.4 cm/s.

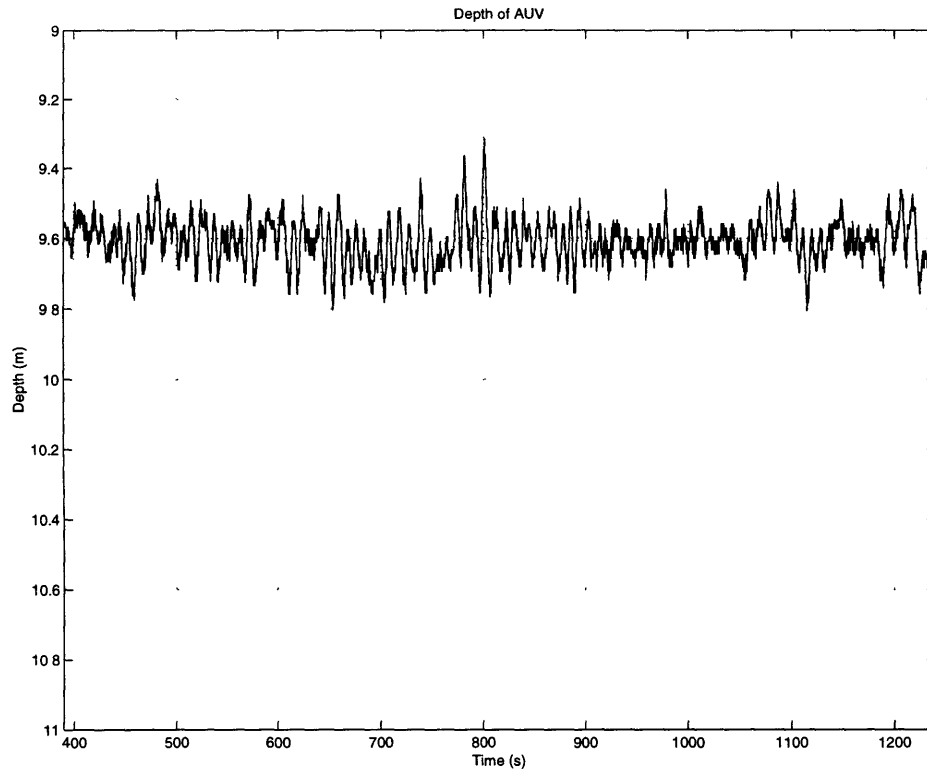


Figure 3.14: Vertical trajectory of the AUV during Mission 11 on June 28, 1996.

Figure 3.17 shows the Earth-referenced horizontal current velocity in the vicinity of the AUV, based on measurements in the first depth bin which was 4 m below the vehicle. Near the vehicle, there existed southeastward current of up to about 0.5 m/s velocity. This result will be compared with that obtained by the method of Kalman filtering in Chapter 4.

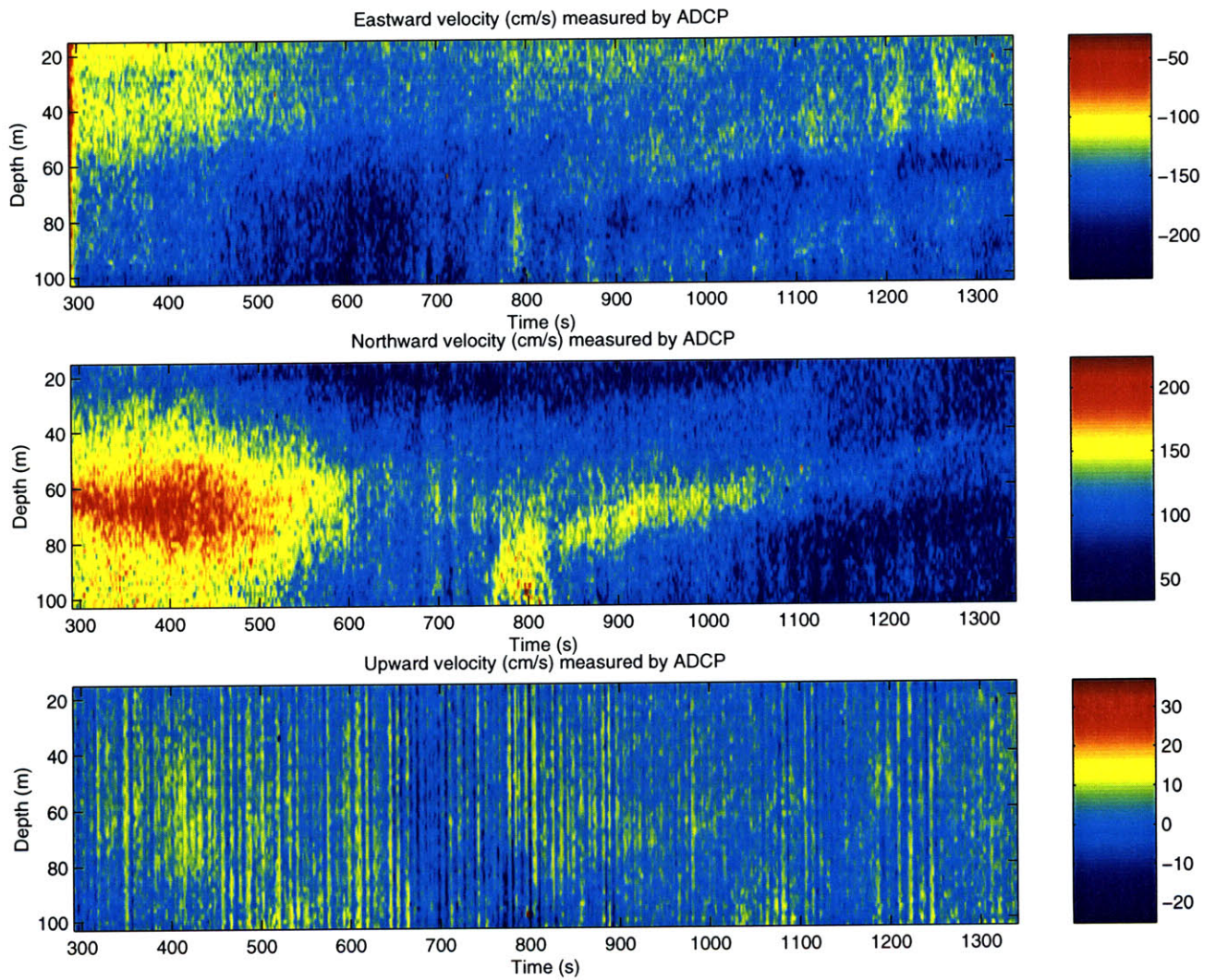


Figure 3.15: Raw current velocity measured by the ADCP during Mission 11 on June 28, 1996.

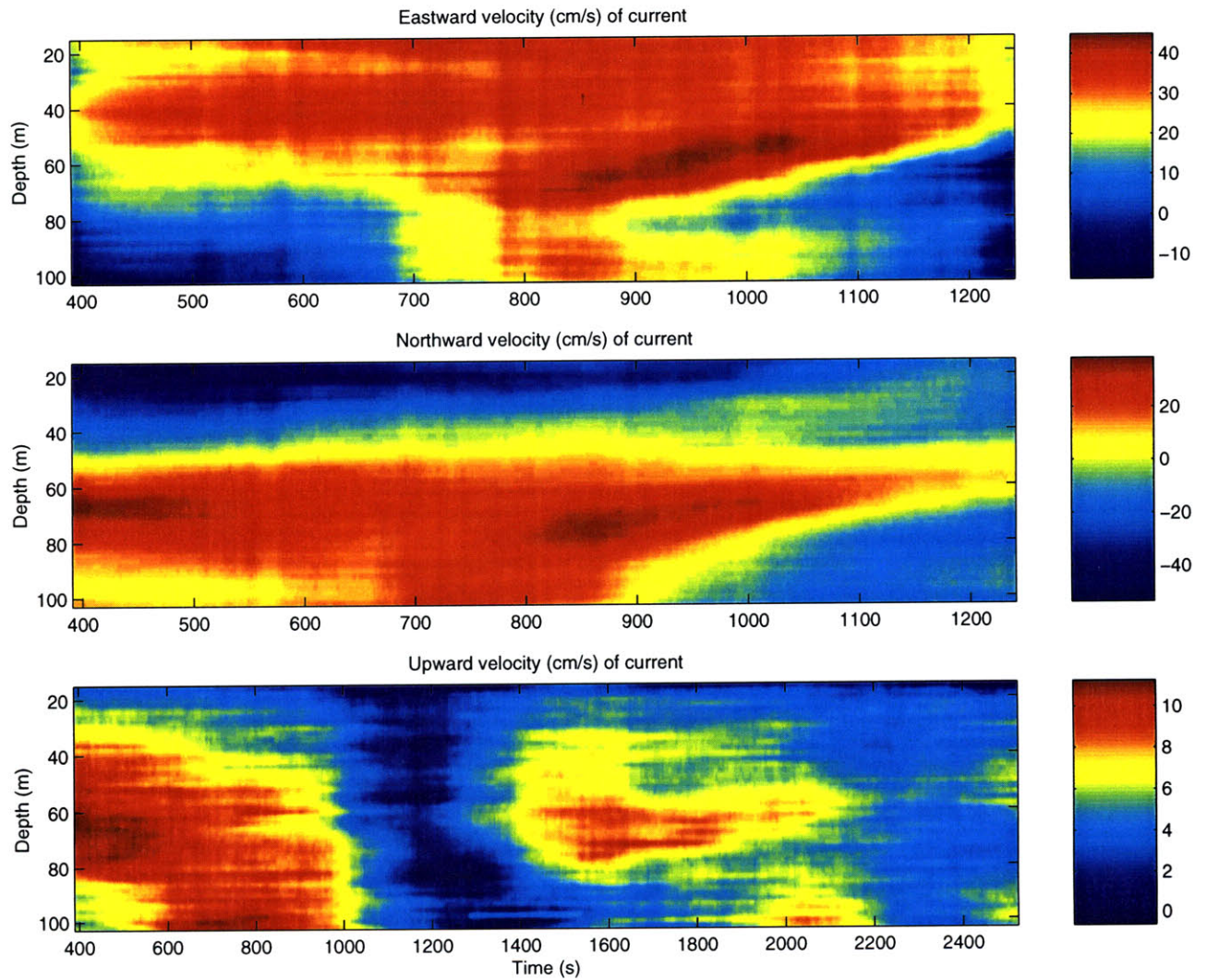


Figure 3.16: Computation result of Earth-referenced current velocity for Mission 11 on June 28, 1996.

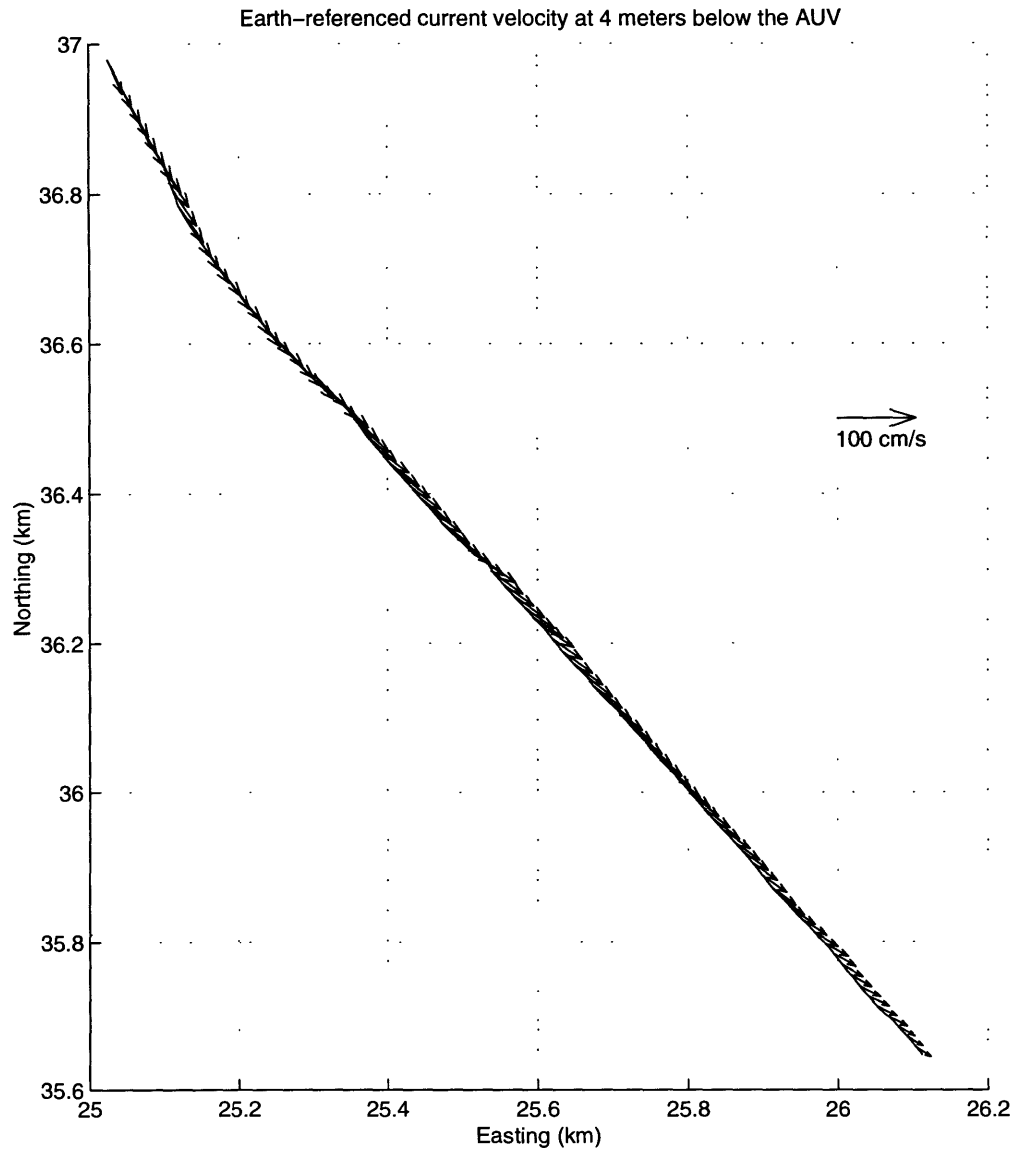


Figure 3.17: Horizontal current velocity near the AUV during Mission 11 on June 28, 1996.

Chapter 4

Application of Extended Kalman Filtering

Water current velocity and AUV's velocity are not two independent quantities. They are interrelated by the current's impact on the vehicle via hydrodynamic forces. For estimating the Earth-referenced current velocity, one step forward is taken in this chapter by utilizing the prior knowledge of the AUV's hydrodynamics [31]. A state space model [32], [19], [33] is established, and the technique of Kalman Filtering is applied. Due to the nonlinearity of the dynamics, an Extended Kalman Filter (EKF) is set up. The filtering algorithm is developed. The Haro Strait Experiment data are used to test the EKF's performance. The result is consistent with the counterpart in Chapter 3. Owing to utilization of hydrodynamic relations, the EKF generates estimates of both current velocity and AUV velocity with good quality. The sacrifice of temporal resolution caused by long smoothing as in Chapter 3 is avoided. The method presented in this chapter provides a real-time algorithm for current velocity extraction from measurements made on a moving platform.

4.1 Brief Introduction to Kalman Filtering

Kalman filtering is an optimal state estimation process that is applied to a dynamic system involving random perturbations [20]. It is a recursive algorithm which gener-

ates the linear least-squares estimate of the system state from noisy data. Kalman filtering has found wide applications in many industrial and military areas such as satellite navigation, video and laser tracking systems, ballistic missile trajectory estimation, etc.

In practice, we are often faced with a state equation and/or a measurement equation that is nonlinear [34]. An approximate optimization solution is achieved by a linearization procedure. The originally linear filtering algorithm is accordingly modified [20]. One such an approach is to make first-order Taylor approximations with the system function at the updated state and with the observation function at the one-step predicted state. The Kalman filter obtained in this way is called Extended Kalman Filter (EKF). The idea to handle a nonlinear model is natural, and the filtering procedure is efficient. Moreover, this recursive algorithm can work in real time.

4.2 Development of Extended Kalman Filter

4.2.1 Model Formulation

We only study the dynamics and estimation problems in the horizontal plane. For the vertical plane, a similar formulation can be derived. The following state space model is established:

$$\text{State equation: } \underline{X}(n+1) = \underline{f}(\underline{X}(n)) + \underline{\xi}(n) \quad (4.1)$$

$$\text{Measurement equation: } \underline{Y}(n) = \underline{C} \underline{X}(n) + \underline{\theta}(n) \quad (4.2)$$

where n is the time index. $\underline{X}(n) = [x(n) \ y(n) \ v_x(n) \ v_y(n) \ v_{xc}(n) \ v_{yc}(n)]^T$ is the 6×1 state vector, where T stands for transpose henceforth. The elements of $\underline{X}(n)$ are

$x(n)$: East position of vehicle (in meter)

$y(n)$: North position of vehicle (in meter)

$v_x(n)$: Earth-referenced eastward velocity of vehicle (in meter/second)

$v_y(n)$: Earth-referenced northward velocity of vehicle (in meter/second)

$v_{xc}(n)$: Earth-referenced eastward velocity of current (in meter/second)

$v_{yc}(n)$: Earth-referenced northward velocity of current (in meter/second)

$\underline{f}(\cdot) = [f_x(\cdot) \ f_y(\cdot) \ f_{vx}(\cdot) \ f_{vy}(\cdot) \ f_{vxc}(\cdot) \ f_{vyc}(\cdot)]^T$ is a 6×1 nonlinear vector function which will be elaborated in Section 4.2.2 and Section 4.2.3.

$\underline{\xi}(n) = [\xi_x(n) \ \xi_y(n) \ \xi_{vx}(n) \ \xi_{vy}(n) \ \xi_{vxc}(n) \ \xi_{vyc}(n)]^T$ is the 6×1 plant noise vector corresponding to the state vector $\underline{X}(n)$.

$\underline{Y}(n) = [x_m(n) \ y_m(n) \ v_{mxrel}(n) \ v_{myrel}(n)]^T$ is the 4×1 measurement vector whose elements are

$x_m(n)$: Measured east position of vehicle (in meter)

$y_m(n)$: Measured north position of vehicle (in meter)

$v_{mxrel}(n)$: Relative eastward velocity measured by the ADCP on board vehicle (in meter/second)

$v_{myrel}(n)$: Relative eastward velocity measured by the ADCP on board vehicle (in meter/second)

$$\underline{C} = \begin{bmatrix} 1 & 0 & 0 & 0 & 0 & 0 \\ 0 & 1 & 0 & 0 & 0 & 0 \\ 0 & 0 & -1 & 0 & 1 & 0 \\ 0 & 0 & 0 & -1 & 0 & 1 \end{bmatrix} \quad (4.3)$$

$\underline{\theta}(n) = [\theta_{xm}(n) \ \theta_{ym}(n) \ \theta_{vmxrel}(n) \ \theta_{vmyrel}(n)]^T$ is the 4×1 measurement noise vector corresponding to the measurement vector $\underline{Y}(n)$.

4.2.2 Underlying Nonlinear Dynamics in Horizontal Plane

As the AUV cruises, it is subjected to drag forces resulting from its relative velocity against the water flow. The schematic is shown in Figure 4.1, where

$$v_{xrel} = v_{xc} - v_x \quad (4.4)$$

$$v_{yrel} = v_{yc} - v_y \quad (4.5)$$

and F_x and F_y are drag forces in x -direction and y -direction respectively. Note that in Figure 4.1, arrow directions for velocity vectors and drag force vectors do not follow the sign convention, in order to intuitively show the actual directions of AUV's and water flow's motion, as well as of the resultant drag forces.

The sign convention for all velocity vectors and for force vectors F_x , F_y , and F_z is: eastward, northward, and upward are positive, and that for force vectors F_1 , F_2 , and F_3 is: forward, to port side, and to top side are positive.

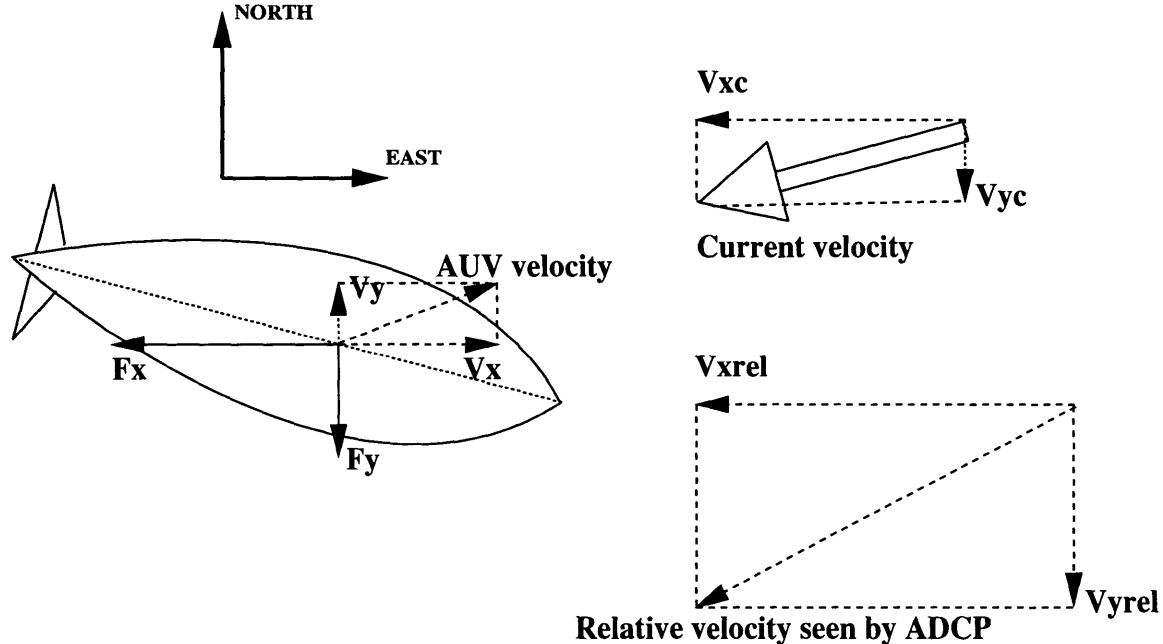


Figure 4.1: Horizontal plane schematic of AUV velocity and water current velocity, as well as resultant drag forces.

More detailed three-dimensional drag force schematic is illustrated in Figure 4.2,

where the relative z -directional velocity is

$$v_{zrel} = v_{zc} - v_z \quad (4.6)$$

Like before, v_{zc} and v_z are the Earth-referenced z -directional velocity of AUV and current, respectively. As will be shown in the following, z -directional velocity's effect on the vehicle's horizontal dynamics is negligible in typical AUV missions. Consequently, they are not included in the state space model. The vector sign convention is strictly followed in Figure 4.2. The vehicle is neutrally buoyant, i.e., its buoyancy cancels out its gravity. Therefore, the major forces on the vehicle are thrust force provided by the propeller and body drag forces. Other forces and torques are not considered yet in the thesis. There are three body drag force components, F_1 : longitudinal (along the vehicle's body), F_2 : lateral in the horizontal plane, and F_3 : lateral in the vertical plane, as shown in Figure 4.2. These forces [35] are functions of v_{mxrel} , v_{myrel} , v_{mzrel} , yaw angle α , and pitch angle β :

$$\begin{aligned} F_1 = & \frac{1}{2}\rho C_{Di} S_l [v_{mxrel} \sin(\alpha) \cos(\beta) + v_{myrel} \cos(\alpha) \cos(\beta) \\ & + v_{mzrel} \sin(\beta)]^2 \text{sign}[v_{mxrel} \sin(\alpha) \cos(\beta) + v_{myrel} \cos(\alpha) \cos(\beta) + v_{mzrel} \sin(\beta)] \\ & + F_{th} \end{aligned} \quad (4.7)$$

$$\begin{aligned} F_2 = & \frac{1}{2}\rho C_{Dt} S_t [-v_{mxrel} \cos(\alpha) \\ & + v_{myrel} \sin(\alpha)]^2 \text{sign}[-v_{mxrel} \cos(\alpha) + v_{myrel} \sin(\alpha)] \end{aligned} \quad (4.8)$$

$$\begin{aligned} F_3 = & \frac{1}{2}\rho C_{Dt} S_t [-v_{mxrel} \sin(\alpha) \sin(\beta) - v_{myrel} \cos(\alpha) \sin(\beta) \\ & + v_{mzrel} \cos(\beta)]^2 \text{sign}[-v_{mxrel} \sin(\alpha) \sin(\beta) - v_{myrel} \cos(\alpha) \sin(\beta) \\ & + v_{mzrel} \cos(\beta)] \end{aligned} \quad (4.9)$$

where F_{th} is thrust force; ρ is water density; C_{Dl} and C_{Dt} are longitudinal and lateral drag coefficients respectively; S_l and S_t are AUV's frontal area and crossflow area respectively.

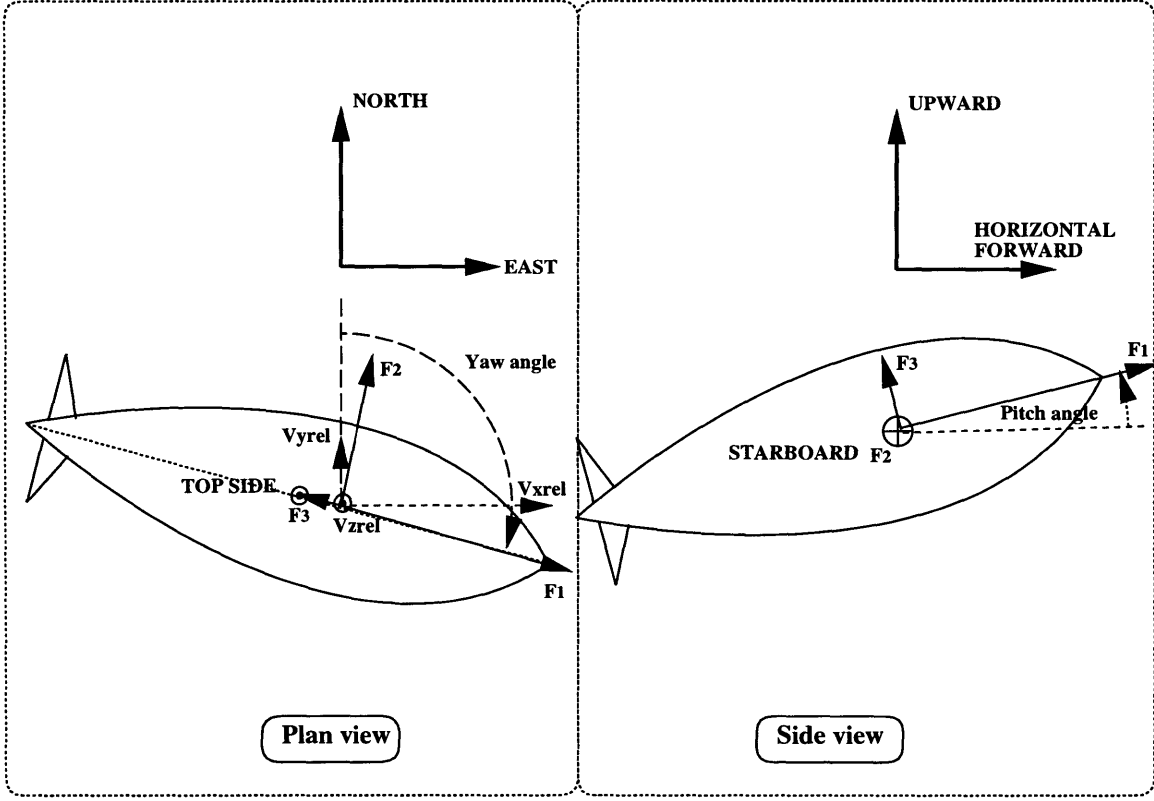


Figure 4.2: Illustration of drag force analysis in both plan view and side view.

F_x , F_y , and F_z are obtained by an orthogonal transformation [36] from F_1 , F_2 , and F_3 :

$$\begin{bmatrix} F_x \\ F_y \\ F_z \end{bmatrix} = \begin{bmatrix} \sin(\alpha)\cos(\beta) & -\cos(\alpha) & -\sin(\alpha)\sin(\beta) \\ \cos(\alpha)\cos(\beta) & \sin(\alpha) & -\cos(\alpha)\sin(\beta) \\ \sin(\beta) & 0 & \cos(\beta) \end{bmatrix} \begin{bmatrix} F_1 \\ F_2 \\ F_3 \end{bmatrix} \quad (4.10)$$

Here we are interested only in the horizontal dynamics of the vehicle, so only F_x and F_y are relevant. In typical AUV missions, during either level legs or yo-yo legs, the vehicle's angle of attack is very small, i.e.,

$$-v_{mxrel}\sin(\alpha)\sin(\beta) - v_{myrel}\cos(\alpha)\sin(\beta) + v_{mzrel}\cos(\beta) \approx 0 \quad (4.11)$$

hence according to Equation (4.9)

$$F_3 \approx 0 \quad (4.12)$$

Furthermore, F_3 's contribution to F_x and F_y is accompanied by a factor of $\sin(\beta)$ where the magnitude of pitch angle β is close to zero in level legs and typically no more than 30° in yo-yo legs. As a result, F_3 's contribution to F_x and F_y is neglected, leading to a simplified calculation of F_x and F_y :

$$\begin{bmatrix} F_x \\ F_y \end{bmatrix} \approx \begin{bmatrix} \sin(\alpha)\cos(\beta) & -\cos(\alpha) \\ \cos(\alpha)\cos(\beta) & \sin(\alpha) \end{bmatrix} \begin{bmatrix} F_1 \\ F_2 \end{bmatrix} \quad (4.13)$$

Correspondingly, AUV's x -directional and y -directional accelerations can be calculated from F_1 and F_2 :

$$\begin{bmatrix} a_x \\ a_y \end{bmatrix} = \begin{bmatrix} \sin(\alpha)\cos(\beta) & -\cos(\alpha) \\ \cos(\alpha)\cos(\beta) & \sin(\alpha) \end{bmatrix} \begin{bmatrix} \frac{F_1}{(m+m_{addl})} \\ \frac{F_2}{(m+m_{addl})} \end{bmatrix} \quad (4.14)$$

where m_{addl} and m_{addt} are AUV's added mass in longitudinal and lateral directions respectively.

Incorporating Equation (4.7) and Equation (4.8) into Equation (4.14), we have

$$\begin{aligned}
a_x = & \frac{1}{m + m_{addl}} \left\{ \sin(\alpha) \cos(\beta) \left\{ \frac{\rho C_{Dt} S_t}{2} (v_{mxrel} \sin(\alpha) \right. \right. \\
& + v_{myrel} \cos(\alpha))^2 \cos^2(\beta) \text{sign}[\cos(\beta) (v_{mxrel} \sin(\alpha) + v_{myrel} \cos(\alpha))] + F_{th} \left. \left. \right\} \right. \\
& - \frac{\rho C_{Dt} S_t}{2(m + m_{addt})} \cos(\alpha) \left\{ -v_{mxrel} \cos(\alpha) \right. \\
& \left. + v_{myrel} \sin(\alpha) \right\}^2 \text{sign}(-v_{mxrel} \cos(\alpha) + v_{myrel} \sin(\alpha)) \left. \right\} \quad (4.15)
\end{aligned}$$

$$\begin{aligned}
a_y = & \frac{1}{m + m_{addl}} \left\{ \cos(\alpha) \cos(\beta) \left\{ \frac{\rho C_{Dt} S_t}{2} (v_{mxrel} \sin(\alpha) \right. \right. \\
& + v_{myrel} \cos(\alpha))^2 \cos^2(\beta) \text{sign}[\cos(\beta) (v_{mxrel} \sin(\alpha) + v_{myrel} \cos(\alpha))] + F_{th} \left. \left. \right\} \right. \\
& + \frac{\rho C_{Dt} S_t}{2(m + m_{addt})} \sin(\alpha) \left\{ -v_{mxrel} \cos(\alpha) \right. \\
& \left. + v_{myrel} \sin(\alpha) \right\}^2 \text{sign}(-v_{mxrel} \cos(\alpha) + v_{myrel} \sin(\alpha)) \left. \right\} \quad (4.16)
\end{aligned}$$

4.2.3 Jacobian Matrix for the Nonlinear State Equation

State equation Equation (4.1) is expanded as

$$x(n+1) = f_x(\underline{X}(n)) + \xi_x(n) = x(n) + v_x(n)\Delta t + \xi_x(n) \quad (4.17)$$

$$y(n+1) = f_y(\underline{X}(n)) + \xi_y(n) = y(n) + v_y(n)\Delta t + \xi_y(n) \quad (4.18)$$

$$v_x(n+1) = f_{vx}(\underline{X}(n)) + \xi_{vx}(n) = v_x(n) + a_x(n)\Delta t + \xi_{vx}(n) \quad (4.19)$$

$$v_y(n+1) = f_{vy}(\underline{X}(n)) + \xi_{vy}(n) = v_y(n) + a_y(n)\Delta t + \xi_{vy}(n) \quad (4.20)$$

$$v_{xc}(n+1) = f_{vxc}(\underline{X}(n)) + \xi_{vxc}(n) = v_{xc}(n) + \xi_{vxc}(n) \quad (4.21)$$

$$v_{yc}(n+1) = f_{vyc}(\underline{X}(n)) + \xi_{vyc}(n) = v_{yc}(n) + \xi_{vyc}(n) \quad (4.22)$$

where Δt is the time interval between adjacent data points.

So the Jacobian matrix for the state dynamics is

$$\frac{\partial f}{\partial \underline{X}(n)} = \begin{bmatrix} 1 & 0 & \Delta t & 0 & 0 & 0 \\ 0 & 1 & 0 & \Delta t & 0 & 0 \\ 0 & 0 & 1 + \frac{\partial a_x(n)}{\partial v_x(n)} \Delta t & \frac{\partial a_x(n)}{\partial v_y(n)} \Delta t & \frac{\partial a_x(n)}{\partial v_{xc}(n)} \Delta t & \frac{\partial a_x(n)}{\partial v_{yc}(n)} \Delta t \\ 0 & 0 & \frac{\partial a_y(n)}{\partial v_x(n)} \Delta t & 1 + \frac{\partial a_y(n)}{\partial v_y(n)} \Delta t & \frac{\partial a_y(n)}{\partial v_{xc}(n)} \Delta t & \frac{\partial a_y(n)}{\partial v_{yc}(n)} \Delta t \\ 0 & 0 & 0 & 0 & 1 & 0 \\ 0 & 0 & 0 & 0 & 0 & 1 \end{bmatrix} \quad (4.23)$$

where the partial derivatives of $a_x(n)$ and $a_y(n)$ with respect to $x(n)$, $y(n)$, $v_x(n)$, $v_y(n)$, $v_{xc}(n)$, and $v_{yc}(n)$ are expanded in the following equations (for tidiness, index n is omitted for $x(n)$, $y(n)$, $v_x(n)$, $v_y(n)$, $v_{xc}(n)$, $v_{yc}(n)$, $\alpha(n)$, and $\beta(n)$):

$$\begin{aligned} \frac{\partial a_x}{\partial v_x} &= -\frac{\rho C_{Dl} S_l}{m + m_{addl}} \sin^2(\alpha) \cos^3(\beta) [(v_{xc} - v_x) \sin(\alpha) \\ &+ (v_{yc} - v_y) \cos(\alpha)] \text{sign}[(v_{xc} - v_x) \sin(\alpha) + (v_{yc} - v_y) \cos(\alpha)] \\ &- \frac{\rho C_{Dt} S_t}{m + m_{addt}} \cos^2(\alpha) [-(v_{xc} - v_x) \cos(\alpha) \\ &+ (v_{yc} - v_y) \sin(\alpha)] \text{sign}[-(v_{xc} - v_x) \cos(\alpha) + (v_{yc} - v_y) \sin(\alpha)] \end{aligned} \quad (4.24)$$

$$\begin{aligned} \frac{\partial a_x}{\partial v_y} &= -\frac{\rho C_{Dl} S_l}{m + m_{addl}} \sin(\alpha) \cos(\alpha) \cos^3(\beta) [(v_{xc} - v_x) \sin(\alpha) \\ &+ (v_{yc} - v_y) \cos(\alpha)] \text{sign}[(v_{xc} - v_x) \sin(\alpha) + (v_{yc} - v_y) \cos(\alpha)] \\ &+ \frac{\rho C_{Dt} S_t}{m + m_{addt}} \sin(\alpha) \cos(\alpha) [-(v_{xc} - v_x) \cos(\alpha) \\ &+ (v_{yc} - v_y) \sin(\alpha)] \text{sign}[-(v_{xc} - v_x) \cos(\alpha) + (v_{yc} - v_y) \sin(\alpha)] \end{aligned} \quad (4.25)$$

$$\frac{\partial a_x}{\partial v_{xc}} = -\frac{\partial a_x}{\partial v_x} \quad (4.26)$$

$$\frac{\partial a_x}{\partial v_{yc}} = -\frac{\partial a_x}{\partial v_y} \quad (4.27)$$

$$\begin{aligned} \frac{\partial a_y}{\partial v_x} = & -\frac{\rho C_{Dl} S_l}{m + m_{addl}} \sin(\alpha) \cos(\alpha) \cos^3(\beta) [(v_{xc} - v_x) \sin(\alpha) \\ & + (v_{yc} - v_y) \cos(\alpha)] \text{sign}[(v_{xc} - v_x) \sin(\alpha) + (v_{yc} - v_y) \cos(\alpha)] \\ & + \frac{\rho C_{Dt} S_t}{m + m_{addt}} \sin(\alpha) \cos(\alpha) [-(v_{xc} - v_x) \cos(\alpha) \\ & + (v_{yc} - v_y) \sin(\alpha)] \text{sign}[-(v_{xc} - v_x) \cos(\alpha) + (v_{yc} - v_y) \sin(\alpha)] \end{aligned} \quad (4.28)$$

$$\begin{aligned} \frac{\partial a_y}{\partial v_y} = & -\frac{\rho C_{Dl} S_l}{m + m_{addl}} \cos^2(\alpha) \cos^3(\beta) [(v_{xc} - v_x) \sin(\alpha) \\ & + (v_{yc} - v_y) \cos(\alpha)] \text{sign}[(v_{xc} - v_x) \sin(\alpha) + (v_{yc} - v_y) \cos(\alpha)] \\ & - \frac{\rho C_{Dt} S_t}{m + m_{addt}} \sin^2(\alpha) [-(v_{xc} - v_x) \cos(\alpha) \\ & + (v_{yc} - v_y) \sin(\alpha)] \text{sign}[-(v_{xc} - v_x) \cos(\alpha) + (v_{yc} - v_y) \sin(\alpha)] \end{aligned} \quad (4.29)$$

$$\frac{\partial a_y}{\partial v_{xc}} = -\frac{\partial a_y}{\partial v_x} \quad (4.30)$$

$$\frac{\partial a_y}{\partial v_{yc}} = -\frac{\partial a_y}{\partial v_y} \quad (4.31)$$

4.2.4 Error Covariance Matrices

Plant noise $\underline{\xi}(n)$ and measurement noise $\underline{\theta}(n)$ are both assumed to be zero-mean white Gaussian vectors. Moreover, the individual variables of $\underline{\xi}(n)$ are considered to be stationary and independent of one another. The covariance matrix of $\underline{\xi}(n)$ is thus diagonal and time invariant:

$$\underline{\Xi}(n) = \underline{\Xi} = \begin{bmatrix} \sigma_x^2 & 0 & 0 & 0 & 0 & 0 \\ 0 & \sigma_y^2 & 0 & 0 & 0 & 0 \\ 0 & 0 & \sigma_{vx}^2 & 0 & 0 & 0 \\ 0 & 0 & 0 & \sigma_{vy}^2 & 0 & 0 \\ 0 & 0 & 0 & 0 & \sigma_{vxc}^2 & 0 \\ 0 & 0 & 0 & 0 & 0 & \sigma_{vyc}^2 \end{bmatrix} \quad (4.32)$$

where the diagonal elements are the variances of corresponding random variables.

Consideration of the covariance matrix of measurement noise

$\underline{\theta}(n) = [\theta_{xm}(n) \ \theta_{ym}(n) \ \theta_{vmxrel}(n) \ \theta_{vmyrel}(n)]^T$ is more complicated. First, let us consider the covariance matrix of random vector $W = AV$ where some zero-mean random vector V has a diagonal covariance matrix Λ_V , and the square matrix A is orthogonal (assuming W , A , and V are all in the real domain). Then the covariance matrix of the zero-mean W is

$$COV_W = E[WW^T] = AE[VV^T]A^T = A\Lambda_V A^T \quad (4.33)$$

If Λ_V is of such a simple form that it can be expressed as

$$\Lambda_V = \sigma^2 I \quad (4.34)$$

where I is the identity matrix, i.e., the diagonal elements of Λ_V are identical, then

$$COV_W = A(\sigma^2 I)A^T = \sigma^2 AA^T = \sigma^2 I = \Lambda_V \quad (4.35)$$

i.e., the covariance matrix of W is equal to that of V .

When the ADCP unit is in an upright orientation, the two orthogonal horizontal

velocity components are calculated by two different pairs of acoustic beams [27]. So the two velocity components can be considered independent. Furthermore, they are of the same error variance [27] so that the error covariance matrix for the two velocity components satisfies Equation (4.34). Eastward and northward velocity in the ENU coordinate system can be transformed from the two local horizontal velocity components using the yaw angle. The transformation matrix is orthogonal. Therefore, with the reasoning described by Equation (4.33), Equation (4.34), and Equation (4.35), we know that $v_{mxrel}(n)$ and $v_{myrel}(n)$ are uncorrelated. If the ADCP unit is tilted from the upright orientation, because of the contribution of ADCP's local vertical velocity component, there would be some correlation between v_{mxrel} and v_{myrel} . In our AUV operations, the vehicle runs either level missions or yo-yo ones with a small pitch angle. Referring to the schematic in Figure 1.1, the ADCP can be considered approximately upright. Hence $v_{mxrel}(n)$ and $v_{myrel}(n)$ are deemed approximately uncorrelated.

$x_m(n)$ and $y_m(n)$ measured by the acoustic LBL navigation system are considered approximately uncorrelated. Certainly, AUV's position measurements $x_m(n)$ and $y_m(n)$ are uncorrelated with ADCP's velocity measurement, because they are provided by different instruments. Therefore, the covariance matrix of measurement noise $\underline{\theta}$ is approximately diagonal and time invariant as well:

$$\underline{\Theta}(n) \approx \underline{\Theta} = \begin{bmatrix} \sigma_{mx}^2 & 0 & 0 & 0 \\ 0 & \sigma_{my}^2 & 0 & 0 \\ 0 & 0 & \sigma_{vmxrel}^2 & 0 \\ 0 & 0 & 0 & \sigma_{vmyrel}^2 \end{bmatrix} \quad (4.36)$$

where the diagonal elements are the variances of corresponding random variables:

$$\sigma_{mx}^2 = \sigma_{my}^2 \text{ and } \sigma_{vmxrel}^2 = \sigma_{vmyrel}^2.$$

4.2.5 Parameter Values

All the parameters to be used are listed and briefly explained in Table 4.1, Table 4.2, and Table 4.3, where “std.” stands for standard deviation.

Table 4.1: AUV related parameters

Parameter	Symbol	Value	Source or Derivation
Data interval	Δt (s)	2	[3]
Water density	ρ (kg/m ³)	1022.5	[15]
Longitudinal drag coefficient	C_{Dl}	0.092	[37]
Lateral drag coefficient	C_{Dt}	0.5	Estimated from FIG. 5.7 of [38]
Frontal area	S_l (m ²)	0.273	$\pi(\frac{0.59}{2} m)^2$ where 0.59 m is the vehicle's biggest diameter
Crossflow area	S_t (m ²)	0.996	$\pi(\frac{0.59}{2} m)(\frac{2.15}{2} m)$ where 2.15 m is the vehicle's length
Mass (including entrained water)	m (kg)	360	[39]
Longitudinal added mass	m_{addl} (kg)	36	[37], [35]
Lateral added mass	m_{addt} (kg)	401	By integration using strip-theory approximation for a slender body [35]
AUV's thrust force	F_{th} (N)	~ 25, slightly mission dependent	Calculated using AUV's average velocity relative to water

Table 4.2: Plant noise parameters

Parameter	Symbol	Value	Source or Derivation
std. error of AUV's x	σ_x (m)	0.2	Traveled distance in Δt at 10% of AUV's representative velocity 1 m/s
std. error of AUV's y	σ_y (m)	0.2	Same as above
std. error of AUV's v_x	σ_{vx} (m/s)	0.1	10% of AUV's representative velocity 1 m/s
std. error of AUV's v_y	σ_{vy} (m/s)	0.1	Same as above
std. error of current's v_{xc}	σ_{vxc} (m/s)	0.05	10% of current's representative velocity 0.5 m/s
std. error of current's v_{yc}	σ_{vyc} (m/s)	0.05	Same as above

Table 4.3: Measurement noise parameters

Parameter	Symbol	Value	Source or Derivation
std. error of AUV's measured x	σ_{mx} (m)	10	[3]
std. error of AUV's measured y	σ_{my} (m)	10	Same as above
std. error of v_{mxrel} measured by ADCP	σ_{vmxrel} (m/s)	0.07	[27]
std. error of v_{myrel} measured by ADCP	σ_{vmyrel} (m/s)	0.07	Same as above

4.3 Extended Kalman Filtering Procedure and Results

4.3.1 Extended Kalman Filtering Procedure

The block diagram of a Kalman filter [19] is shown in Figure 4.3. As expressed by Equation (4.1), the plant dynamics involves nonlinear functions. Therefore, we use an EKF which linearizes the problem about a trajectory that is continuously updated with state estimates resulting from measurements [19]. Only the first-order dynamics is retained during each update and predict cycle, hence Jacobian matrices as in Equation (4.23) are used to establish the linearized dynamics at each step.

For the model formulated by Equation (4.1) and Equation (4.2), the procedure of Extended Kalman Filtering (EKF) can be summarized in the following [33], [40]. Note that in Equation (4.1), function $\underline{f}(\cdot)$ is only on $\underline{X}(n)$ while the plant noise $\xi(n)$ is additive.

1. Initialization of state and error covariance:

$$\hat{\underline{X}}(0|-1) = E[\underline{X}(0)] \quad (4.37)$$

$$\underline{\Sigma}(0|-1) = cov[\underline{X}(0); \underline{X}(0)] \quad (4.38)$$

$$n = 0 \quad (4.39)$$

2. Compute Kalman filter gain:

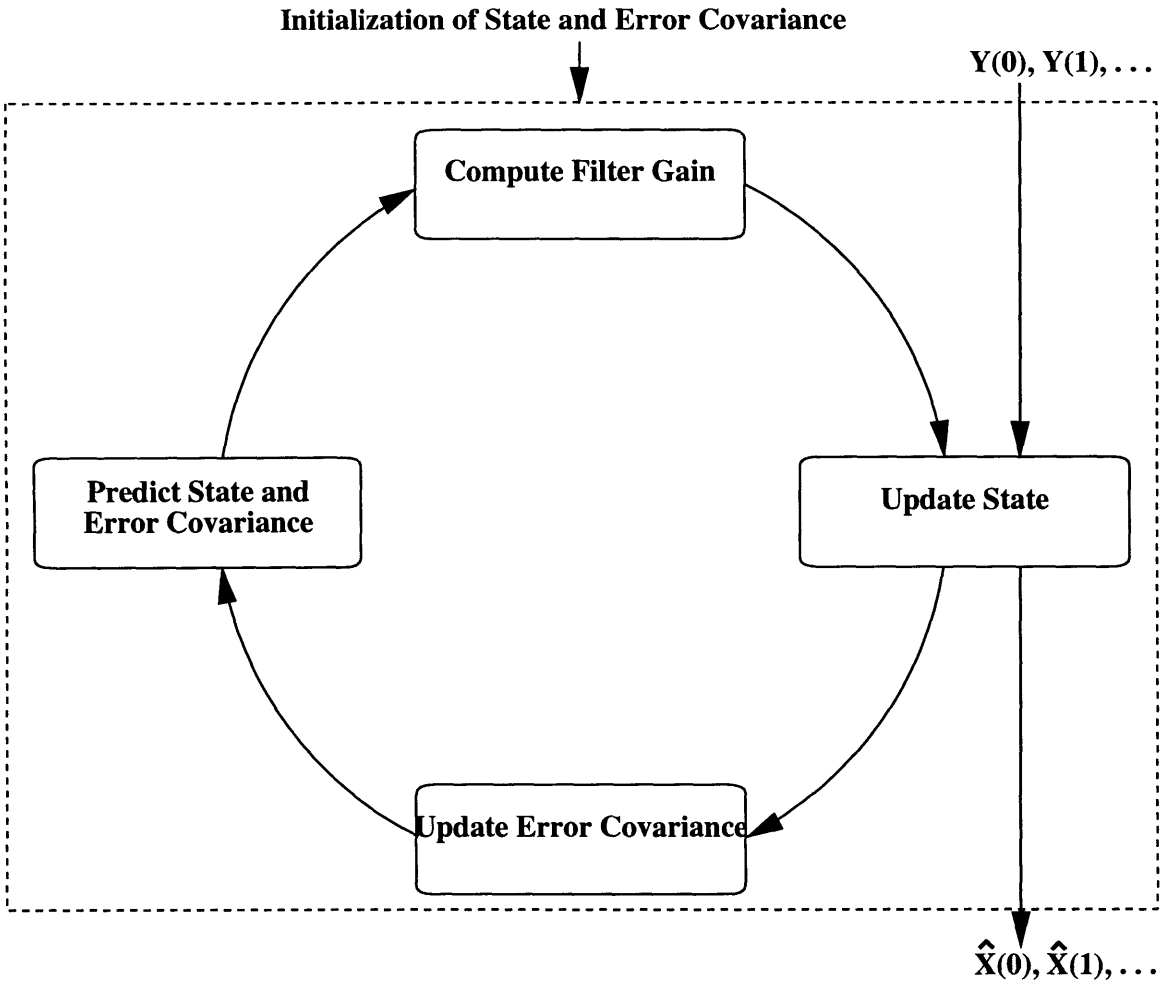


Figure 4.3: Kalman filter loop.

$$\underline{H}(n) = \underline{\Sigma}(n|n-1)\underline{C}^T[\underline{C}\underline{\Sigma}(n|n-1)\underline{C}^T + \underline{\Theta}]^{-1} \quad (4.40)$$

3. Update state:

$$\underline{\hat{X}}(n|n) = \underline{\hat{X}}(n|n-1) + \underline{H}(n)[\underline{Y}(n) - \underline{C}\underline{\hat{X}}(n|n-1)] \quad (4.41)$$

4. Update error covariance:

$$\underline{\Sigma}(n|n) = \underline{\Sigma}(n|n-1) - \underline{H}(n)\underline{C}\underline{\Sigma}(n|n-1) \quad (4.42)$$

5. Predict state and error covariance:

$$\underline{\hat{A}}(n) = \left. \frac{\partial \underline{f}}{\partial \underline{X}(n)} \right|_{\underline{X}(n)=\underline{\hat{X}}(n|n)} \quad (4.43)$$

$$\underline{\hat{X}}(n+1|n) = \underline{f}(\underline{\hat{X}}(n|n)) \quad (4.44)$$

$$\underline{\Sigma}(n+1|n) = \underline{\hat{A}}(n)\underline{\Sigma}(n|n)\underline{\hat{A}}^T(n) + \underline{\Xi}(n) \quad (4.45)$$

where Equation (4.43) is evaluated using Equation (4.23).

6. Increase n and go to step 2.

In the initialization step, the state and the error covariance matrix is assigned as in the following:

$$x(0| - 1) = \text{the first } x_m \text{ measured by the LBL system} \quad (4.46)$$

$$y(0| - 1) = \text{the first } y_m \text{ measured by the LBL system} \quad (4.47)$$

$$v_x(0| - 1) = -(\text{the first } v_{mxrel} \text{ measured by the ADCP}) \quad (4.48)$$

$$v_y(0| - 1) = -(\text{the first } v_{myrel} \text{ measured by the ADCP}) \quad (4.49)$$

$$v_{xc}(0| - 1) = 0 \quad (4.50)$$

$$v_{yc}(0| - 1) = 0 \quad (4.51)$$

$$\underline{\Sigma}(0| - 1) = \begin{bmatrix} \sigma_{mx}^2 & 0 & 0 & 0 & 0 & 0 \\ 0 & \sigma_{my}^2 & 0 & 0 & 0 & 0 \\ 0 & 0 & \sigma_{vmxrel}^2 & 0 & 0 & 0 \\ 0 & 0 & 0 & \sigma_{vmyrel}^2 & 0 & 0 \\ 0 & 0 & 0 & 0 & \sigma_{vmxrel}^2 & 0 \\ 0 & 0 & 0 & 0 & 0 & \sigma_{vmyrel}^2 \end{bmatrix} \quad (4.52)$$

4.3.2 Current and AUV Velocity Estimation Results

Field data of the Haro Strait Experiment are used to test the presented EKF algorithm. ADCP data correction has been done as in Chapter 3. Results on AUV Mission 11 on June 28 are shown here. This mission has been introduced in Section 3.2. Note that v_{mxrel} and v_{myrel} are data from the ADCP's first depth bin which was 4 m below the vehicle. The first-bin measurements were made so close to the AUV that they are considered to represent the water current that applied hydrodynamic forces on the vehicle.

Estimation output of the six state processes, $x(n)$, $y(n)$, $v_x(n)$, $v_y(n)$, $v_{xc}(n)$, and v_{yc} are shown in Figure 4.4 and Figure 4.5, where they are compared with corresponding raw measurements. In Figure 4.4, EKF estimates are very close to the raw measurements, but differences would show up when zoomed in. Figure 4.5 demonstrates that Earth-referenced current velocity can be reconstructed from raw relative velocity measured by the ADCP and AUV positions measured by the LBL navigation

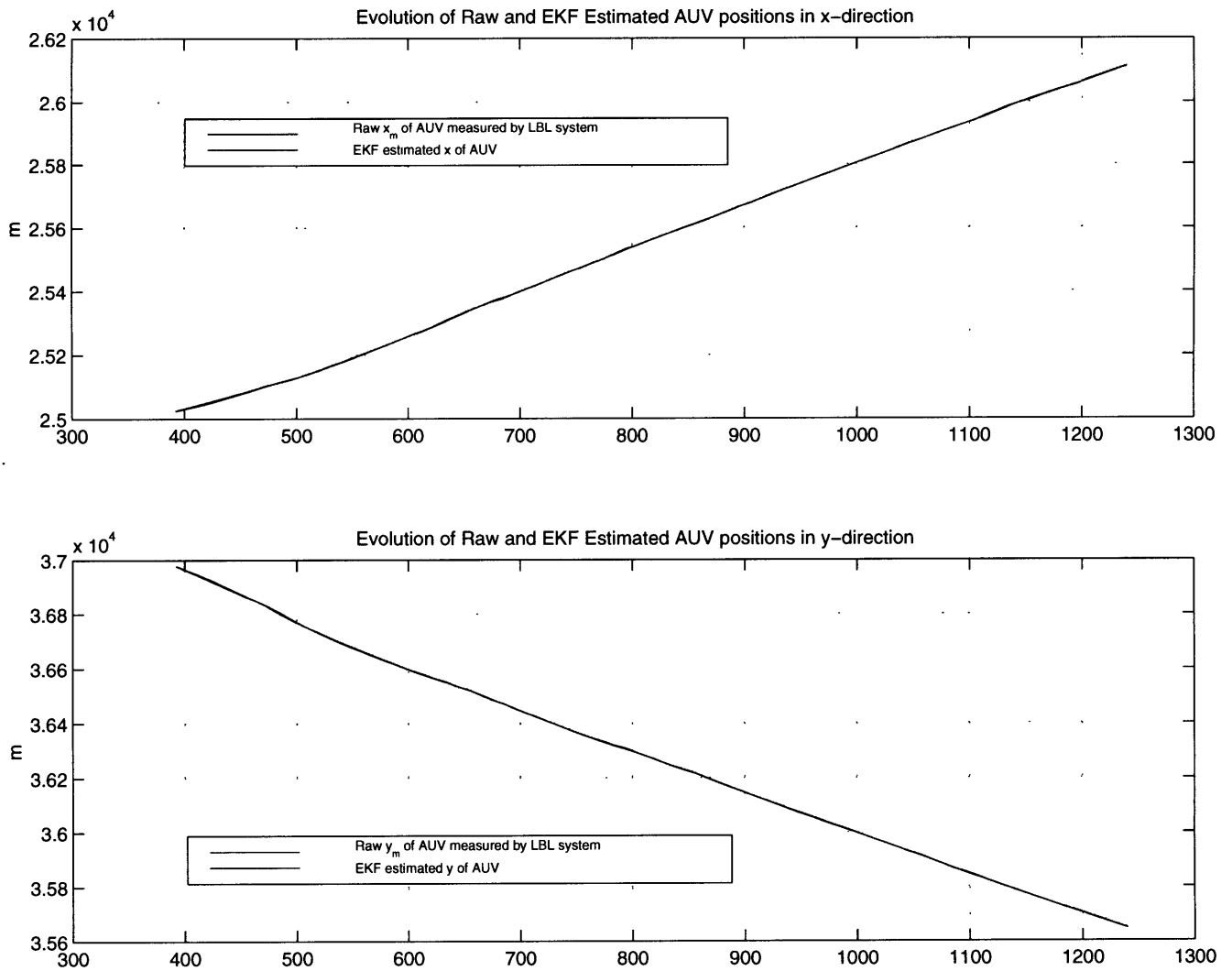


Figure 4.4: EKF-estimated AUV positions compared with raw measurements made by the LBL navigation system.

system, by utilizing the underlying dynamics expressed by the EKF model. Meanwhile, Earth-referenced AUV velocity is also estimated, as a much needed by-product.

Convergence performance of the EKF is shown by Figure 4.6. In less than 100 s (equivalent to 50 data points with a 2-second interval), the filter reaches the steady state. The position estimation error decreases from the initial 10 m to about 3.6 m (note: $\sigma_{11}(0|-1) = 10$ m, but $\sigma_{11}(0|0) = 7.1$ m appears as the initial value in Figure 4.6). Velocity estimation errors are about 0.18 m/s at steady state. This value is larger than the ADCP's instrument noise 0.07 m/s. The reason is that the large uncertainty of raw position measurements translates into the velocity uncertainty. Note

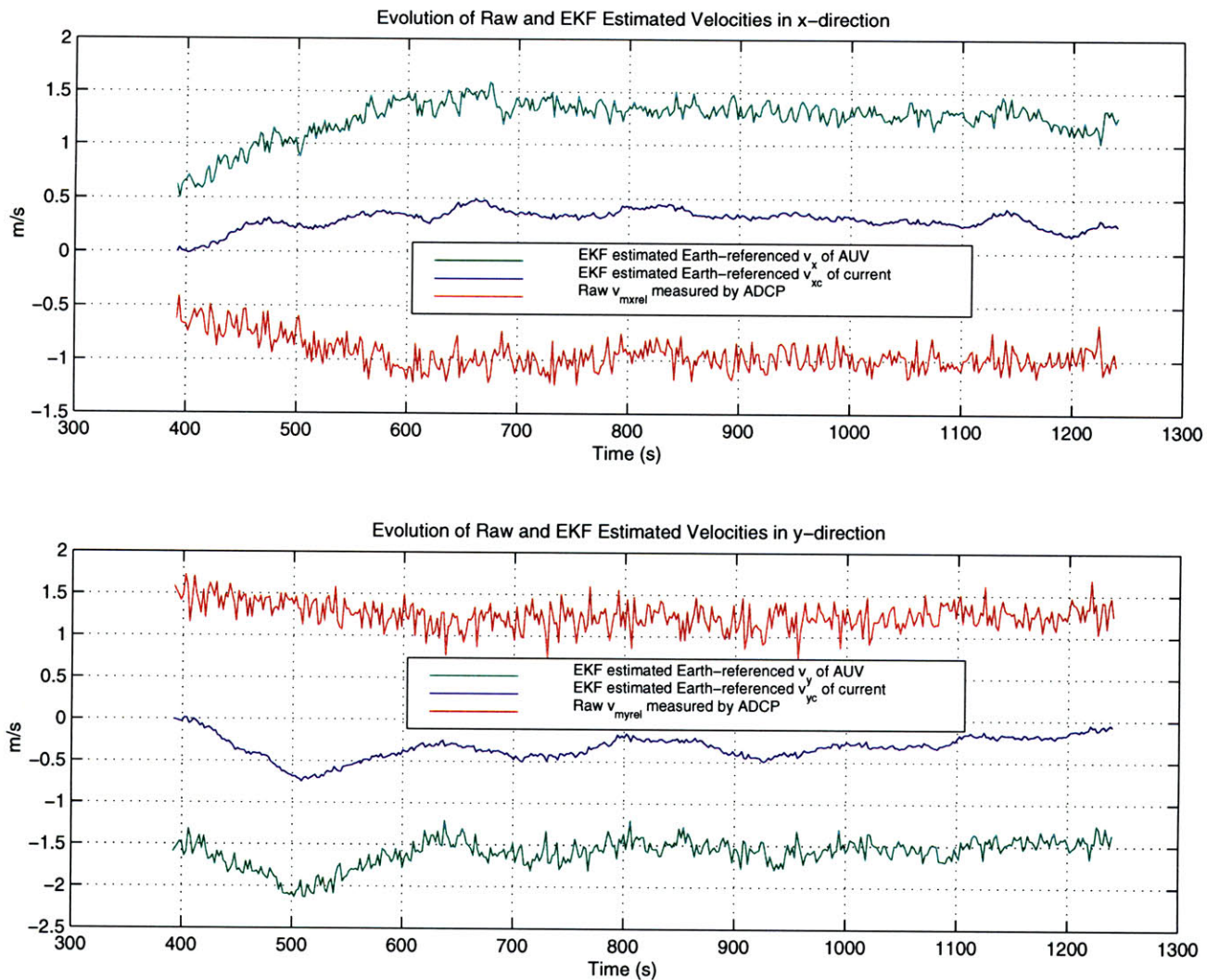


Figure 4.5: EKF-estimated AUV's and current's Earth-referenced velocities compared with raw velocity measurement made by the ADCP.

that in this EKF algorithm, no smoothing window is used. If a 200-second smoothing window were to be further applied as was done in producing horizontal current velocities shown in Figure 3.16, the estimation error would be reduced to 1.8 cm/s which is only one-third of the 5 cm/s error given by the post-processing method in Chapter 3. Square roots of absolute values of two pairs of cross-correlation terms in the covariance matrix are shown in Figure 4.7, on the same scale as the lower panel of Figure 4.6. The coupling errors between velocity pairs appear to be very small, indicating that the assumption on plant noise is acceptable.

Kalman filter gains are illustrated in Figure 4.8 and Figure 4.9. The 5th row

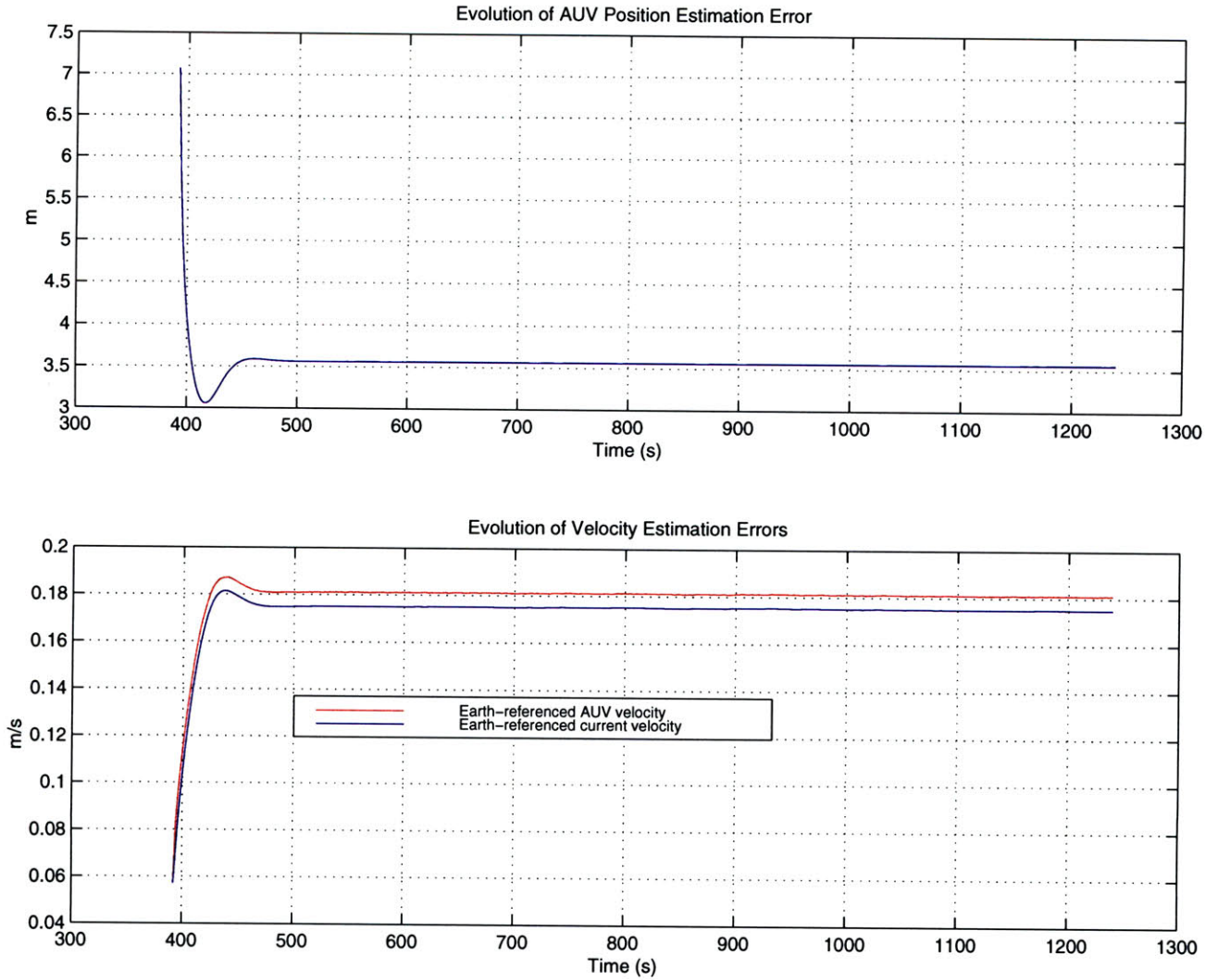


Figure 4.6: Time evolution of Kalman Filter estimation errors for AUV’s position, AUV’s Earth-referenced velocity, and current’s Earth-referenced velocity.

and the 6th row of the 6×4 gain matrix H are shown in Figure 4.8 and Figure 4.9, respectively. Let us take Figure 4.8 for a close look. This 4-element row represents the influence weights of the 4 measurements on the estimation of x -directional Earth-referenced current velocity v_{xc} . At steady state, $H(5, 3)$ and $H(5, 1)$ have much larger magnitude than the other two elements. This means that x -directional measurements v_{mxrel} and x_m have much larger effects than y -directional measurements v_{myrel} and y_m . A corresponding observation is made with y -directional Earth-referenced current velocity v_{yc} , as shown in Figure 4.9. These observations make very good physical sense.

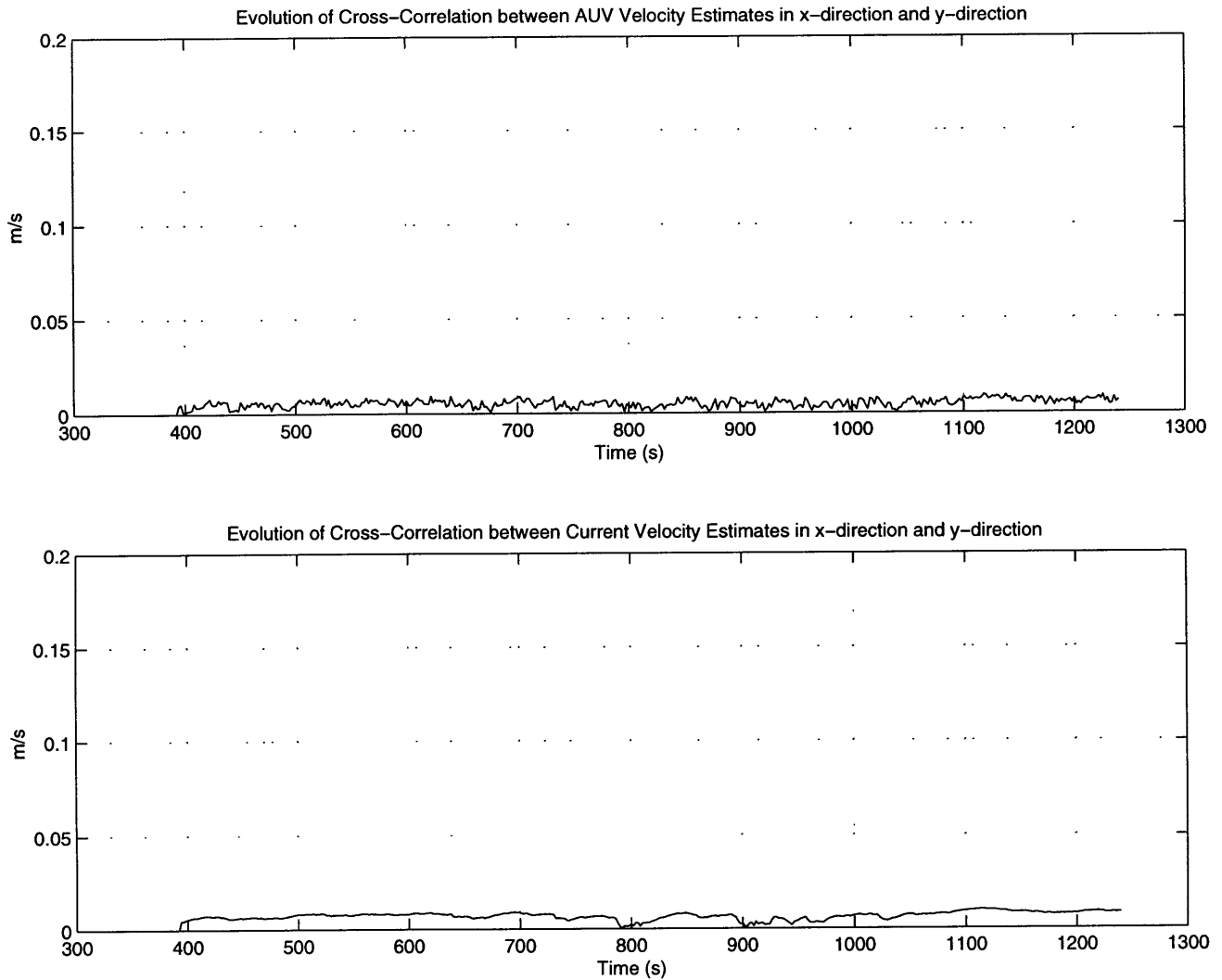


Figure 4.7: Time evolution of cross-correlations for AUV’s Earth-referenced velocity pair and current’s Earth-referenced velocity pair.

At last, Earth-referenced horizontal current velocity is drawn on the AUV’s horizontal trajectory, as shown in Figure 4.10. Note that only one velocity data point out of every five is used to make arrows more legible. We can see that during this AUV mission, there was a southeast current with velocity of up to about 0.5 m/s. This is consistent with the result shown in Figure 3.17 in Chapter 3 for the same mission. We should be able to decrease the discrepancy between Figure 3.17 and Figure 4.10 by improving the Kalman Filter model as will be discussed in Section 5.2. One of the advantages of utilizing Kalman filtering is that long smoothing window is no longer necessary. Thus temporal resolution is maintained. Such a causal algorithm can be

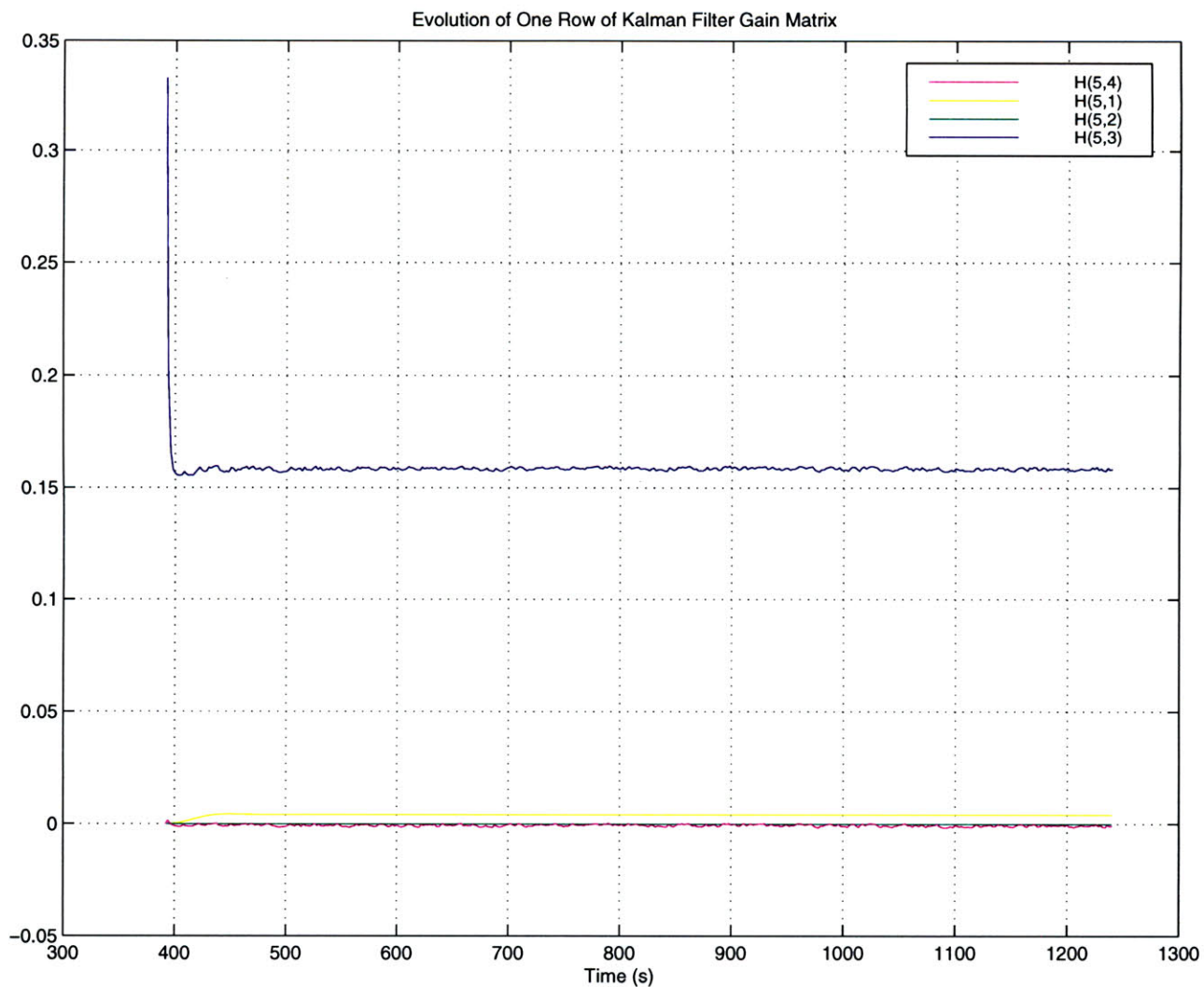


Figure 4.8: Time evolution of Kalman Filter gains for current's Earth-referenced v_{xc} associated with the 4 measurements: x_m , y_m , v_{mxrel} , and v_{myrel} .

implemented in real time, which is a very useful feature for AUV applications.

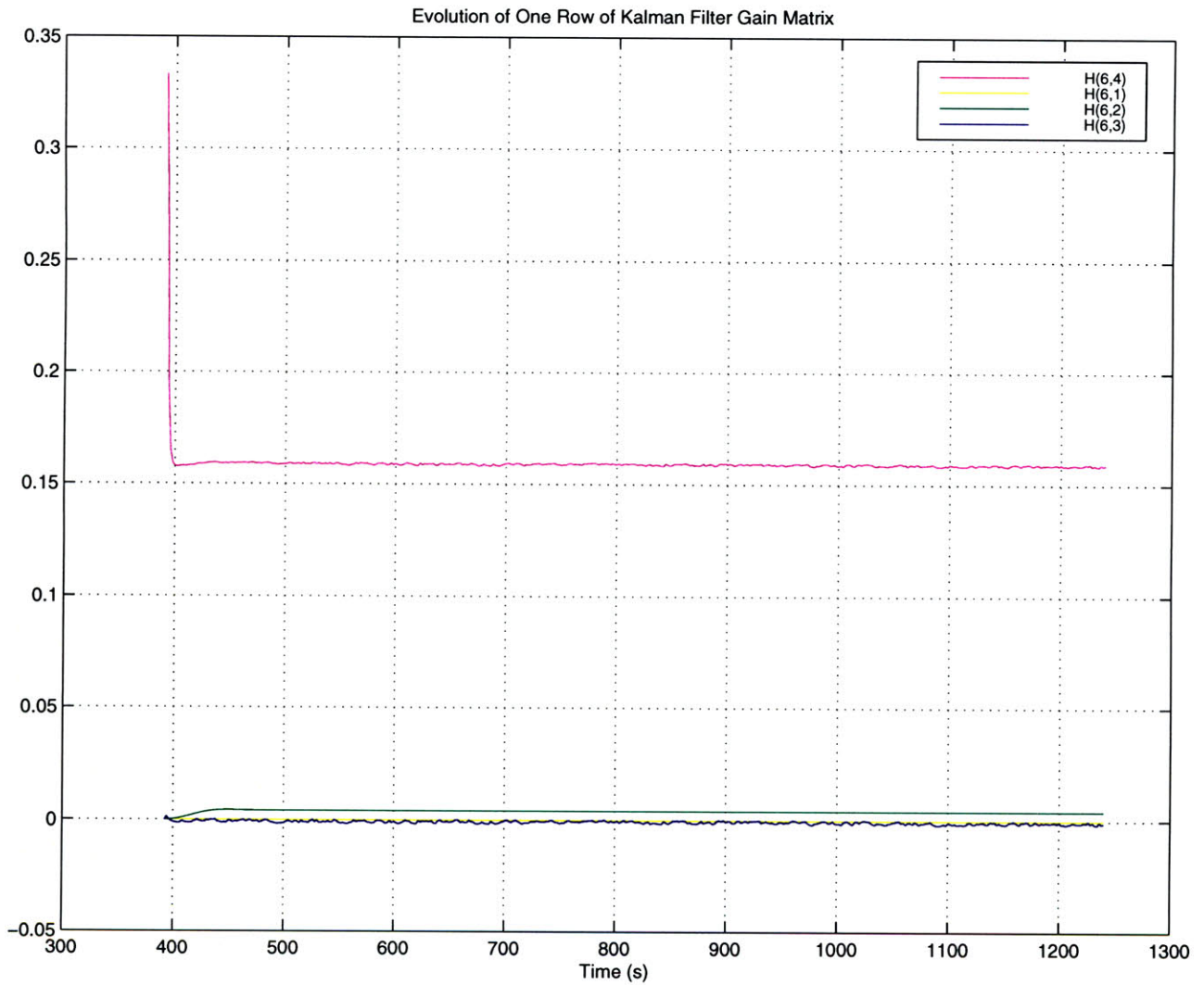


Figure 4.9: Time evolution of Kalman Filter gains for current's Earth-referenced v_{yc} associated with the 4 measurements: x_m , y_m , v_{mzrel} , and v_{myrel} .

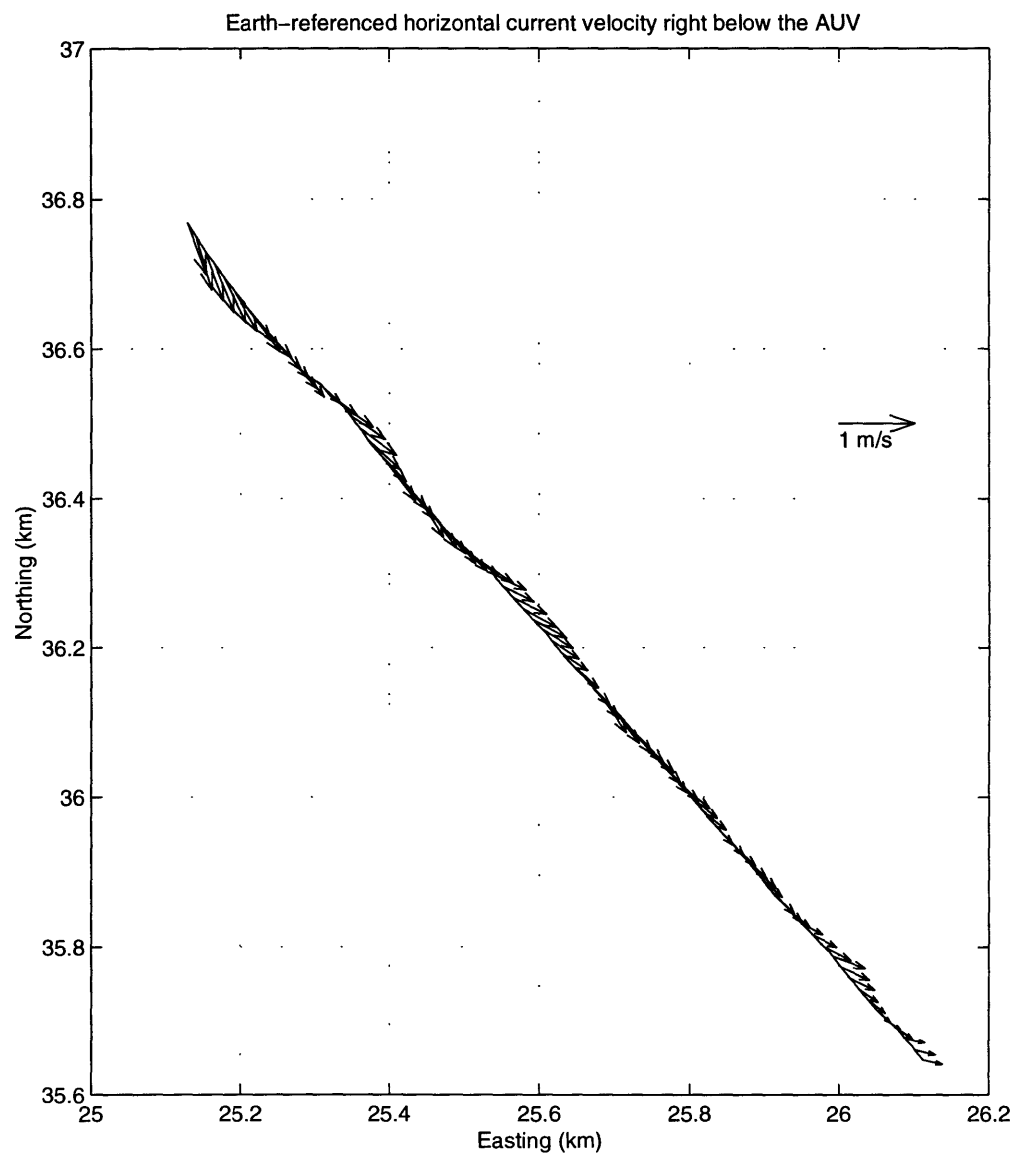


Figure 4.10: Earth-referenced horizontal current velocity near the AUV during Mission 11 on June 28, 1996.

Chapter 5

Conclusion

5.1 Contributions

Water current velocity is of key importance to ocean process research, environmental monitoring, ship traffic control, and other offshore work. The thesis presents an AUV-borne current velocity profiling system, and the methods for recovering the Earth-referenced current velocity from ADCP measurements made on a moving platform. To the author's knowledge, this system is the first to map current velocity from an AUV. The contributions are summarized as follows.

1. A data post-processing scheme for extracting Earth-referenced current velocity from raw ADCP measurements is presented. LBL navigation data and depth measurements for the AUV are used to estimate the vehicle's own velocity. The vehicle's velocity is removed from the relative current velocity made by the ADCP. Earth-referenced current velocity is thus extracted. Heading/pitch/roll correction for the ADCP data is conducted.
2. A framework for current velocity estimation utilizing Extended Kalman Filtering (EKF) is developed. The hydrodynamics connecting current velocity and vehicle's motion is utilized. A state space model is set up to represent the AUV's nonlinear dynamics under hydrodynamic forces. By closely following the dynamics, velocity estimation noise of the EKF is lower than that given by the

post-processing method. Application of EKF also leads to a causal algorithm for measuring water current from an AUV in real time.

3. Field data from the Haro Strait Tidal Front Experiment are processed by both algorithms. The resultant Earth-referenced current velocity reveals horizontal layered structure as well as alternating upwellings and downwellings in the tidal mixing process. Horizontal current velocity is also consistent with the vehicle's deviated trajectory.

5.2 Future Work

1. After the Haro Strait Experiment, bottom-track mode was added to the RDI Workhorse ADCP. In this mode ADCP calculates its own velocity referenced to the bottom and its distance from the bottom, when the bottom is within its range. Bottom-track can be utilized to improve estimates of the AUV's velocity. Modifications to the current velocity extraction algorithms should be accordingly made.
2. The AUV's horizontal velocity can directly be estimated by using the travel times for each LBL transponder. This is probably a better approach than differentiating the LBL fix data. The effect of the LBL array calibration errors would be suppressed by using travel time differentiations.
3. The technique of EKF is applied for extracting Earth-referenced current velocity. Chapter 4 builds the framework, while the presented algorithm is only for the horizontal plane. For the vertical plane, a similar formulation can be derived. On the other hand, more delicate AUV dynamics, such as angular rotation, should be included for a more precise description of its motion. More precise dynamics representation will consequently improve the current velocity estimate.

Bibliography

- [1] A. J. Williams III, “Historical overview: Current measurement technologies”, *IEEE Oceanic Engineering Society Newsletter*, pp. 5–9, Spring 1998.
- [2] J. G. Bellingham, C. A. Goudey, T. R. Consi, J. W. Bales, and D. K. Atwood, “A second generation survey AUV”, in *Proc. IEEE Symposium on Autonomous Underwater Vehicle Technology*, Cambridge, MA, July 1994, pp. 148–156.
- [3] J. G. Bellingham, B. A. Moran, Y. Zhang, J. S. Willcox, N. Cruz, R. Grieve, J. J. Leonard, and J. W. Bales, “Haro Strait Experiment 1996 MIT Sea Grant Component”, Technical Report, MIT Sea Grant AUV Lab, 1997.
- [4] R. L. Gordon, “Acoustic Doppler Current Profiler principles of operation - a practical primer”, Tech. Rep., RD Instruments, San Diego, CA, January 1996.
- [5] P. E. Plimpton, H. P. Freitag, and M. J. McPhaden, “ADCP velocity errors from pelagic fish schooling around equatorial moorings”, *Journal of Atmospheric and Oceanic Technology*, vol. 14, pp. 1212–1223, October 1997.
- [6] R. F. Marsden and Y. Gratton, “A method for correcting vertical velocities measured from a vessel-mounted Acoustic Doppler Current Profiler”, *Journal of Atmospheric and Oceanic Technology*, vol. 14, pp. 1533–1538, February 1997.
- [7] M. G. G. Foreman and H. J. Freeland, “A comparison of techniques for tidal removal from ship-mounted acoustic Doppler measurements along the southwest coast of Vancouver Island”, *Journal of Geophysical Research*, vol. 96, no. C9, pp. 17007–17021, 1991.

- [8] Hahnel, “A note on the use of Acoustic Doppler Current Profilers in mesoscale surveys”, *IEEE Journal of Oceanic Engineering*, vol. 16, no. 4, pp. 368–373, October 1991.
- [9] C. N. Flagg, G. Schwartz, E. Gottlieb, and T. Rossby, “Operating an Acoustic Doppler Current Profiler aboard a container vessel”, *Journal of Atmospheric and Oceanic Technology*, vol. 15, pp. 257–271, February 1998.
- [10] J. Fischer and M. Visbeck, “Deep velocity profiling with self-contained ADCPs”, *Journal of Atmospheric and Oceanic Technology*, vol. 10, pp. 764–773, October 1993.
- [11] F. Schott, M. Visbeck, and J. Fischer, “Observations of vertical currents and convection in the central Greenland Sea during the winter of 1988-1989”, *Journal of Geophysical Research*, vol. 98, no. C8, pp. 14401–14421, August 1993.
- [12] F. Schott and W. Johns, “Half-year-long measurements with a buoy-mounted Acoustic Doppler Current Profiler in the Somali Current”, *Journal of Geophysical Research*, vol. 92, no. C5, pp. 5169–5176, 1987.
- [13] K. Pulkkinen, “Comparison of different bin-mapping methods for a bottom-mounted acoustic profiler”, *Journal of Atmospheric and Oceanic Technology*, vol. 10, pp. 404–409, 1993.
- [14] D. E. Leader, “Kalman filter estimation of underwater vehicle position and attitude using a Doppler velocity aided inertial motion unit”, Ocean Engineer thesis, Massachusetts Institute of Technology, September 1994.
- [15] J. G. Bellingham, “New oceanographic uses of autonomous underwater vehicles”, *Marine Technology Society Journal*, vol. 31, no. 3, pp. 34–47, Fall 1997.
- [16] E. R. Levine, D. N. Connors, R. R. Shell, and R. C. Hanson, “Autonomous underwater vehicle-based hydrographic sampling”, *Journal of Atmospheric and Oceanic Technology*, vol. 14, pp. 1444–1454, 1997.

- [17] A. L. Meyrowitz, D. R. Blidberg, and R. C. Michelson, “Autonomous vehicles”, *Proceedings of the IEEE*, vol. 84, no. 8, pp. 1147–1164, August 1996.
- [18] Y. Zhang and J. S. Willcox, “Current velocity mapping using an AUV-borne Acoustic Doppler Current Profiler”, *Proc. 10th International Symposium on Unmanned Untethered Submersible Technology*, pp. 31–40, September 1997, Durham, NH.
- [19] R. G. Brown and P. Y. C. Hwang, *Introduction to Random Signals and Applied Kalman Filtering with MATLAB Exercises and Solutions*, New York, NY: John Wiley and Sons, 1997.
- [20] C. K. Chui and G. Chen, *Kalman Filtering with Real-Time Applications*, New York, NY: Springer-Verlag, 1991.
- [21] D. M. Farmer, E. A. D’Asaro, M. V. Trevorrow, and G. T. Dairiki, “Three-dimensional structure in a tidal convergence front”, *Continental Shelf Research*, vol. 15, no. 13, pp. 1649–1673, 1995.
- [22] E. A. Thomson, “Experiment will use sound pulses to probe tidal mixing”, *MIT Tech Talk*, pp. 6–7, May 1996.
- [23] M. G. G Foreman, R. A. Walters, and R. F. Henry, “A model for simulating currents in eastern Juan de Fuca Strait and the southern Strait of Georgia”, *Proc. IEEE Oceans’93*, vol. 1, pp. 335–340, 1993.
- [24] M. G. G Foreman, R. A. Walters, R. F. Henry, C. P. Keller, and A. G. Dolling, “A tidal model for eastern Juan de Fuca Strait and the southern Strait of Georgia”, *Journal of Geophysical Research*, vol. 100, no. C1, pp. 721–740, 1995.
- [25] H. Schmidt, J. G. Bellingham, M. Johnson, D. Herold, D. M. Farmer, and R. Pawlowicz, “Real-time frontal mapping with AUVs in a coastal environment”, *Proc. MTS/IEEE Oceans’96*, pp. 1094–1098, September 1996.

- [26] SonTek, San Diego, CA, *Acoustic Doppler Velocimeter (ADV) Principles of Operation*, October 1996.
- [27] RD Instruments, San Diego, CA, *Acoustic Doppler Current Profiler Workhorse Technical Manual*, April 1996.
- [28] B. H. Brumley, R. G. Cabrera, K. L. Deines, and E. A. Terray, “Performance of a broad-band Acoustic Doppler Current Profiler”, *IEEE Journal of Oceanic Engineering*, vol. 16, no. 4, pp. 402–407, October 1991.
- [29] Paroscientific, Inc., Redmond, WA, *Digiquartz Precision Pressure Instruments - Programming and Operation Manual*, July 1995.
- [30] KVH Industries, Inc., Middletown, RI, *KVH Digital Gyro Compass and KVH Digital Gyro Inclinator - Technical Manual*, October 1994.
- [31] Y. Zhang, “Application of extended Kalman filtering to current velocity measurement from an autonomous underwater vehicle”, Term paper for course 6.433 (Recursive Estimation), MIT Department of Ocean Engineering, May 1998.
- [32] A. Gelb, Ed., *Applied Optimal Estimation*, Cambridge, MA: MIT Press, 1974.
- [33] M. Athans, “Recursive estimation (course 6.433) lecture notes”, MIT Department of Electrical Engineering and Computer Science, 1998.
- [34] S. M. Kay, *Fundamentals of Statistical Signal Processing: Estimation Theory*, Englewood Cliffs, NJ: Prentice-Hall, Inc, 1993.
- [35] J. N. Newman, *Marine Hydrodynamics*, Cambridge, MA: MIT Press, 1977.
- [36] G. Strang, *Introduction to Applied Mathematics*, Wellesley, MA: Wellesley-Cambridge Press, 1986.
- [37] F. Hover, “Physical Modeling of the Odyssey II Vehicle”, Technical Report, MIT Sea Grant Program and Woods Hole Oceanographic Institution, 1995.

- [38] R. H. Sabersky, Ed., *Fluid Flow*, New York, NY: Macmillan Publishing Company, 1989.
- [39] J. W. Bales, “Odyssey IIB parameter calculations”, Personal communications, MIT Sea Grant AUV Lab, 1998.
- [40] A. S. Willsky, G. W. Wornell, and J. H. Shapiro, “Stochastic processes, detection, and estimation (course 6.432) lecture notes”, MIT Department of Electrical Engineering and Computer Science, 1997.